Cellular mechanisms of heterogeneity in *NF2*-mutant schwannoma

Christine Chiasson-MacKenzie[1,2], Jeremie Vitte[3], Ching-Hui Liu[1,2], Emily A. Wright[1,2], Elizabeth A. Flynn[1,4], Shannon L. Stott[1,4], Marco Giovannini[3] and Andrea I. McClatchey[1,2*]

[1]Massachusetts General Hospital Cancer Center, Harvard Medical School, 149 13th Street, Charlestown, MA 02129, USA

[2]Department of Pathology, Massachusetts General Hospital, Harvard Medical School, 55 Fruit Street, Boston, Massachusetts, 02114, USA

[3]Department of Head and Neck Surgery, David Geffen School of Medicine at UCLA and Jonsson Comprehensive Cancer Center (JCCC), University of California Los Angeles, Los Angeles, CA 90095, USA

[4]Center for Engineering in Medicine and BioMEMS Resource Center, Surgical Services, Massachusetts General Hospital, Harvard Medical School, 114 16th Street, Charlestown, Massachusetts, 02129, USA

*Correspondence: mcclatch@helix.mgh.harvard.edu

Abstract

Schwannomas are common sporadic nervous system tumors and diagnostic features of familial neurofibromatosis type 2 (NF2) that develop predominantly on cranial and spinal nerves and cause severe neurological deficits and significant morbidity. Virtually all schwannomas result from inactivation of the *NF2* tumor suppressor gene with few, if any, cooperating mutations. Despite their genetic uniformity schwannomas exhibit remarkable clinical and therapeutic heterogeneity, which has impeded the success of early rational therapies. An understanding of how heterogeneity develops in *NF2*-mutant schwannomas is critically needed to improve therapeutic options for these patients. We have found that loss of the membrane:actin cytoskeleton-associated NF2 tumor suppressor protein, merlin, yields unstable intrinsic polarity and enables *Nf2*$^{-/-}$ Schwann cells to adopt distinct programs of coordinated ErbB ligand production and polarized signaling, suggesting a self-generated model of schwannoma heterogeneity. We validated the heterogeneous distribution of biomarkers of these programs in human schwannoma tissue and took advantage of the synchronous development of multiple lesions in a well-studied mouse model to establish a quantitative pipeline that can be used to study how schwannoma heterogeneity evolves and impacts nerve function and therapeutic response in mouse, and ultimately human schwannomas. Our studies inform a mounting appreciation that intrinsic mechanisms are major contributors to heterogeneity across many human cancers.

Introduction

Schwannomas account for a large proportion of sporadic nervous system tumors in humans and are hallmarks of the inherited tumor predisposition syndrome neurofibromatosis type 2 (NF2)[1-4]. Although usually benign, schwannomas develop predominantly on spinal nerve roots and cranial nerves, causing significant neurological deficit, chronic pain, and morbidity. Few targeted therapies have been developed to treat schwannomas and instead, high-risk

surgical removal is often necessary. This is particularly difficult for NF2 patients, who frequently develop multiple, recurring tumors.

Whether inherited or sporadic, virtually all schwannomas are caused by genetic inactivation of the *NF2* tumor suppressor gene, and few cooperating mutations have been identified[5]. Despite being genetically 'cold', schwannomas exhibit surprising intertumoral heterogeneity, including remarkably variable natural histories, growth rates and clinical impact, even within the same NF2 patient[1]. Neither growth rate or tumor burden correlates with the ability of schwannomas to cause pain or nerve dysfunction, and the few rational therapies that have been evaluated for schwannoma have yielded at best a heterogeneous and cytostatic response, often followed by accelerated tumor regrowth after drug cessation[6-8]. An understanding of the molecular basis of schwannoma heterogeneity is essential for the development of successful non-surgical therapies.

Intratumoral heterogeneity is evident histologically and ultrastructurally in schwannoma[9-11]. Hematoxylin and eosin staining of schwannoma tissue reveals regions of spindle-shaped cells that form concentric whorls or aligned arrays, and others of more radially-shaped cells with shorter cell processes. Ultrastructurally, cells within schwannomas exhibit striking variation in the extent of cell-cell versus cell-basal lamina contact, with apposing cell surfaces coated with dense basal lamina or forming interlocking cell-cell contacts in widely varying proportions, and some regions featuring denuded basal lamina, prominent vacuoles and microcysts[9]. Such 'Antoni A and B' regions exhibit different patterns of immune infiltration and vascularity, suggesting that they harbor distinct paracrine environments[12]. These visible features of cellular heterogeneity vary from tumor to tumor as features of intertumoral heterogeneity, but it is not known how they are established within otherwise genetically homogeneous tumors.

Schwann cells (SCs) are uniquely polarized epithelial cells that can transition between a bipolar, migratory state during development and wound repair, and an apicobasally polarized state that relies on heterotypic contact with the neuron as an extrinsic spatial polarity cue[13-15]. Rather than the discrete junctional and fluid-exposed apical surfaces of conventional epithelia,

apicobasally polarized SCs form a hybrid 'apicojunctional' adaxonal surface that is dedicated to contacting the neuron, enriched in both apical and cell-cell adhesion proteins, and a crucial site of neuroglial signaling between the two cell types[16-20]. The remaining abaxonal surface contacts basal lamina that is generated by the SCs themselves. Importantly, signaling at the two SC surfaces is distinct[14]. For example, neuregulin 1 (Nrg1) that is tethered to the neuronal plasma membrane activates ErbB3 on the adaxonal SC surface to induce mammalian target of rapamycin complex 1 (mTORC1)-triggered phosphorylation of S6rp and expansion of the neuron-ensheathing membrane edge, while laminin signaling to α6-containing integrins promotes mTORC2-dependent activation of serum and glucocorticoid-induced kinase 1 (SGK1) and phosphorylation of its effector NDRG1 abaxonally[14,21-23]. Notably, laminin-activated feedback limits Nrg1-ErbB3-driven membrane production at the adaxonal surface, suggesting that the size of the two signaling domains is normally under feedback control via unknown mechanisms[21]. *In vivo* SC polarity is initiated and spatially defined by contact with the neuronal cell membrane but *in vitro* it is imposed and sized by attachment to a laminin-coated culture dish. In schwannomas, the spatial cues that normally govern polarized signaling are lost, and cells exhibit strikingly variable polarized surface content.

The *NF2*-encoded tumor suppressor, merlin, and closely related plasma membrane:cytoskeleton linking ERM proteins (ezrin, radixin, moesin) share interdependent roles in organizing the cell cortex and govern intrinsic cell polarity in many contexts[24-31]. For example, in single matrix-embedded epithelial cells, merlin-deficiency impairs the spatial restriction of cortical ezrin that normally polarizes the cell; instead, ectopic cortical ezrin drives unstable intrinsic polarity[27]. The importance of controlling ERM activity is underscored by recent studies demonstrating the role of ERM-mediated membrane:cytoskeleton linkage in gating stem cell pluripotency[32,33]. Consistent with such fundamental cell cortex-organizing activities, merlin and the ERMs influence many signaling programs, including the activity of small GTPases of the Rho and Ras families, the Hippo signaling network and mTOR kinases[34-38]. Merlin/ERM proteins also modulate the cytoskeletal response to members of the ErbB family of tyrosine kinase

receptors[39-45]. For example, in liver epithelial cells merlin deficiency enhances the excitability of the cortical cytoskeleton to Epidermal Growth Factor (EGF) stimulation in an ezrin-dependent manner, enabling macropinocytosis, an actin-based mechanism of nutrient scavenging that is initiated by large cell surface ruffles[40,46]. Through fundamental roles in organizing the cell cortex, merlin and the ERM proteins are poised to enable the coordination of intrinsic polarity with other fundamental cellular activities.

We have found that NF2-deficient SCs exhibit unstable polarity and can adopt distinct phenotypic states featuring coordinated auto/paracrine ErbB ligand and polarity gene expression and polarized cytoskeletal organization, suggesting a novel model of self-generated heterogeneity that could explain the notoriously variable clinical and therapeutic behaviors of schwannomas. Importantly, this model also suggests new biomarkers of schwannoma heterogeneity that we validated *in vivo* using a quantitative imaging pipeline that we have developed. Our findings provide mechanistic insight into the adaptive biology of SCs, new biomarkers, and a quantitative imaging platform that can be developed to guide the treatment of human schwannoma; they also inform studies of intrinsic heterogeneity in other tumor types.

Results

Nf2-deficient SCs exhibit altered intrinsic polarity and exaggerated cortical responses to Nrg1

When cultured on laminin-coated tissue culture dishes, *Nf2*$^{flox/flox}$ (WT) SCs are bipolar with small ruffles forming at the poles, reflecting intrinsic polarity that is independent of cues imposed by axonal contact (Fig. 1A,B). In contrast, three different primary mouse *Nf2*$^{flox/flox}$ SC populations in which *Nf2* has been acutely deleted (hereafter denoted *Nf2*$^{-/-}$; Supplementary Fig. 1A) exhibited a loss of this intrinsic polarity, instead featuring multiple dynamically extending processes containing larger ruffles, as has been reported (Fig. 1A,B)[47]. Multipolarity in *Nf2*$^{-/-}$ SCs is accompanied by a more radial cell shape and distribution of actin, compared to the long parallel stress fibers exhibited by bipolar WT SCs (Fig. 1C; Supplementary Fig. 1B). This is

consistent with the fundamental role for merlin in establishing intrinsic cortical polarity that has been observed in many cell types[27,29].

Nrg1 regulates SC proliferation, migration, and myelination, and is normally included in SC culture medium[13,48,49]. When deprived of Nrg1, *Nf2*$^{-/-}$ SCs exhibited a striking enhancement of basally positioned and radially distributed ezrin-containing microvilli relative to WT SCs (Fig. 1D,E, Supplementary Fig. 1C)[50]. On the other hand, acute stimulation of *Nf2*$^{-/-}$ SCs with Nrg1 yielded a dramatic loss of microvilli and reorganization of ezrin and actin to form a circumferential band from which large cortical ruffles emanated (Fig. 1D-G; Supplementary Fig. 1B,C). WT SCs exhibit only weak cortical ruffles and ezrin relocalization in response to Nrg1, despite activating similar levels of downstream signals (Fig. 1D-G; Supplementary Fig. 1B,D). Depletion of ezrin eliminated both multipolarity and the exaggerated cytoskeletal responses to Nrg1 availability in *Nf2*$^{-/-}$ SCs (Fig. 1H; Supplementary Fig. 1E-G)[40]. These data are consistent with a model wherein in *Nf2*$^{-/-}$ SCs, ectopic cortical ezrin drives multipolarity and distinct exaggerated cytoskeletal responses to the presence (ruffles) or absence (microvilli) of Nrg1, enabling heterogeneous cytoskeletal states.

Progressive junctional ruffling and adhesion in *Nf2*$^{-/-}$ SCs in the presence of Nrg1

Like the axon-facing 'apicojunctional' surface of normal SCs *in vivo*, cortical ruffles exhibited by *Nf2*$^{-/-}$ SCs in the presence of Nrg1 contain the adherens junction proteins N-cadherin and β-catenin, the Nrg1 receptor ErbB3 and its heterodimeric partner ErbB2 (Fig. 2A-B, Supplementary Fig. 2A-D)[51-53]. In fact, ErbB2, ErbB3, and the key ErbB3 effector pAkt are enriched in ruffles in *Nf2*$^{-/-}$ SCs compared to WT SCs, despite similar levels of total ErbB2, ErbB3, pAkt and pERK (Supplementary Fig. 1C, 2A-E). Moreover, in contrast to WT SCs that restrict N-cadherin-based cell-cell contacts to bipolar cell tips, *Nf2*$^{-/-}$ SCs progressively make stable adhesive contacts around their entire periphery, from which cortical ruffles emerge (Fig. 2A,B). At late confluence *Nf2*$^{-/-}$ SCs form tightly packed adhesive aggregates that eventually lose attachment to the laminin-coated culture dish as spheroids (Fig. 2C, Supplementary Fig.

2F). In contrast, WT SCs do not adhere to one another, and instead undergo contact inhibition of locomotion (CIL), during which they redirect their movement after collision until confluence when they round up as individual cells (Fig. 2D,E; Supplementary Fig. 2F, Supplementary Movie 1 and 2)[54]. Notably, WT and *Nf2*$^{-/-}$ SCs express similar levels of *N-cadherin* (*Cdh2*) and of *Sox2*, which can induce relocalization of N-cadherin to SC contacts, and little E-cadherin (Supplementary Fig. 2G,H)[53], suggesting that *Nf2*-deficiency does not drive increased adhesion by these mechanisms. Thus, in the presence of Nrg1 *Nf2*-deficiency enables the progressive expansion of an adhesive 'apicojunctional' ErbB signaling compartment.

Growth factor stimulated cortical actin ruffles can trigger macropinocytosis, a form of extracellular nutrient engulfment that is a signature of *Nf2*-deficiency in other cell types[40,46]. Indeed, in the presence of Nrg1, *Nf2*$^{-/-}$ but not WT SCs exhibit uptake of the macropinocytic cargo dextran-488 that is blocked by the macropinocytosis inhibitor 5-(N-ethyl-N-isopropyl) amiloride (EIPA) (Fig. 2F-H). Upon internalization, dextran-488 can be observed in large macropinosome-like vesicles adjacent to ruffling cell-cell contacts (Supplementary Fig. 3A). Murine *Nf2*-mutant schwannoma cells also exhibited striking Nrg1-stimulated ruffling and EIPA-sensitive dextran-488 uptake that was reversed by *Nf2* re-expression or ezrin depletion (Supplementary Fig. 3B-J). Importantly, *in vivo* and *ex vivo* approaches revealed prominent EIPA-sensitive dextran-TMR uptake in schwannomas arising in the well-established *Postn-Cre;Nf2*$^{flox/flox}$ mouse model (Fig. 2I-K; see below)[55]. This observation could have immediate therapeutic ramifications as large macrotherapeutics largely gain entry into cells via macropinocytosis[56]. As one example, extracellular vesicles (EVs) can be engineered to deliver many therapeutic cargoes, including nucleic acids for gene replacement[57-59]. We found that *Nf2*$^{-/-}$ schwannoma cells readily take up EVs in an EIPA-sensitive manner (Fig. 2L). These data suggest that cells in schwannomas can exhibit exaggerated cortical ruffling and tumor-selective uptake of macrotherapeutics in the presence of Nrg1, but when Nrg1 is not available, instead adopt a basally oriented cytoskeleton and exhibit neither ruffling or macropinocytosis.

***Nf2*$^{-/-}$ SCs develop auto/paracrine heterogeneity**

In vivo, the unrestricted expansion of cell-cell contact, junctional Nrg1-signaling and cortical ruffling exhibited by cultured *Nf2*$^{-/-}$ SCs would occur when intercellular contact is permitted and Nrg1 is available. However, cells within schwannomas do not retain axonal contact and must adapt to the loss of axonally provided Nrg1. We reasoned that *Nf2*$^{-/-}$ SCs might adapt by producing their own Nrg1, like other tumors that deploy autocrine ErbB ligand expression to induce cortical ruffling and macropinocytic scavenging[60]. We found that Nrg1 deprivation did yield modestly increased *Nrg1* expression in both WT and *Nf2*$^{-/-}$ SCs but caused a dramatic upregulation of the EGFR-specific ligands *Tgfa and Egf* specifically in *Nf2*$^{-/-}$ SCs (Fig. 3A,B). Surprisingly however, although EGF ligands trigger cortical ruffles and macropinocytosis in many cell types, including *Nf2*$^{-/-}$ liver epithelial cells[40,60], both EGF and TGFα suppress these phenotypes in *Nf2*$^{-/-}$ SCs, and instead enhance basal actin stress fibers and ezrin-containing basally oriented microvilli (Fig. 3C-E, Supplementary Fig. 4A; compare to Fig. 1D-G)[50]. In fact, Nrg1-deprived *Nf2*$^{-/-}$ SCs also upregulated multiple components of the SC basal signaling platform, including laminin (*Lama2*), the laminin receptors α6 integrin (*Itga6*) and α-dystroglycan (*Dag1*), and collagen (*Col1a2*) consistent with the enhanced basal cytoskeletal organization seen under conditions of Nrg1-deprivation (Fig. 3F; Supplementary Fig. 4B)[14]. Both Nrg1-deprived WT and *Nf2*$^{-/-}$ SCs also upregulated *Egfr*, which is normally expressed at low levels in SCs but is often increased in schwannomas, some of which respond clinically to pharmacologic EGFR inhibition (Supplementary Fig. 4C)[6,7,61]. Wild-type SCs neither upregulate EGF ligands nor ruffle in response to them (Fig. 3B; Supplementary Fig. 4D). Thus, *Nf2*$^{-/-}$ SCs may adapt to Nrg1-deprivation by upregulating an EGFR-associated basal polarity program.

In addition to Nrg1, peripheral nerves provide nutrients to adjacent SCs and vice versa. An important example may be the glutamate-glutamine cycle that is well-studied in the central nervous system[62,63]. In other types of tumors, glutamine depletion induces autocrine ruffling and macropinocytosis[60]. Indeed, we found that in *Nf2*$^{-/-}$ SCs glutamine depletion strongly induces ruffling and dextran-488 uptake that is blocked by the pan-ErbB inhibitor afatinib (ErbBi; Fig. 4A;

Supplementary Fig. 5 A,B). Consistent with the ability of Nrg1 but not TGFα or EGF to induce ruffling, the expression of *Nrg1 (type I)*, but not *Tgfa* is dramatically enhanced under these conditions (Fig. 4B; Supplementary Fig. 5C,E). Glutamine deprivation did not affect ErbB receptor levels or the levels of *Nrg2* or *Nrg3* (not detected) (Supplementary Fig. 5D,E). Conditioned medium from glutamine-deprived *Nf2*$^{-/-}$ SCs induced ruffling and EIPA- and ErbBi-sensitive dextran-488 uptake, while conditioned medium from Nrg1-deprived *Nf2*$^{-/-}$ SCs, like recombinant TGFα or EGF, enhanced basal structures (Fig. 4C-E, Supplementary Fig. 5F). Notably, *Nrg1* upregulation was completely rescued by the addition of exogenous glutamate (Fig. 4F). Altogether these data suggest that *Nf2*-deficient SCs can activate auto/paracrine programs of Nrg1-driven apicojunctional signaling and macropinocytic scavenging or EGF ligand-driven basal signaling in the absence of nutrients normally provided by axons.

Heterogeneous mTOR activation and drug sensitivity

In normal SCs *in vivo* axonal Nrg1 drives the polarized activation of mTORC1, as measured by pS6 levels[14]. Aberrant mTORC1 signaling has been implicated in schwannoma, but the pharmacologic mTOR inhibitor everolimus (mTORi), one of the only drug-based therapies being evaluated in schwannoma patients, has yielded variable and cytostatic results thus far[36,37,64,65]. Our studies suggest that pS6 may be a specific biomarker of Nrg1 but not TGFα production in schwannoma. Indeed, pS6 levels are elevated in nutrient-starved Nrg1-expressing *Nf2*$^{-/-}$ but not WT SCs (Fig. 5A,B). Moreover, treatment of *Nf2*$^{-/-}$ SCs with conditioned medium from glutamine-deprived Nrg1-expressing *Nf2*$^{-/-}$ SCs dramatically stimulated pS6 while medium from Nrg1-deprived, TGFα-expressing *Nf2*$^{-/-}$ SCs dramatically lowered pS6 levels (Fig. 5C). Importantly, however, we found that high *Nrg1*-expressing, pS6+ *Nf2*$^{-/-}$ SCs are *resistant* to mTORi relative to Nrg1-deprived, *Tgfa*-expressing pS6- *Nf2*$^{-/-}$ SCs, and mTORi has no impact on *Nrg1* expression and instead reduces *Tgfa* expression (Fig. 5D,E, Supplementary Fig. 6). On the other hand, ErbBi blocks *Nrg1* but not *Tgfa* expression (Fig. 5F). These results could explain the cytostatic and heterogeneous clinical efficacy of mTORi, as well as the 'rebound' tumor

growth that is often seen upon cessation of mTORi treatment and could be triggered by a reservoir of accumulated Nrg1[64,65]. These data have important ramifications for designing and interpreting therapeutic strategies for schwannoma and beg an investigation of the distribution of these biomarkers in tumor tissue.

Self-generated heterogeneity

Collectively, our observations suggest that when deprived of axonal signals, *Nf2*$^{-/-}$ SCs can adopt different programs of coordinated ligand production and cytoskeletal polarity, featuring high *Nrg1* expression, high pS6 levels and apicojunctional polarity dominated by cortical actin ruffling and macropinocytosis, or high *Tgfa* expression, low pS6 and basal polarity dominated by basal actin stress fibers and ECM receptors (Fig 6A,B). The progressive ligand- and ECM-associated features of *Nf2*$^{-/-}$ SC 'states' could enable self-generated patterns of heterogeneity within schwannomas. To test this possibility, we developed a three-dimensional (3D) model in which single *Nf2*$^{-/-}$ SCs are embedded in inert polyethylene glycol (PEG) hydrogels in the absence of the polarity cues imposed by a laminin-coated surface in standard two-dimensional SC culture[66]. After 4 days of culture in the presence of Nrg1, single *Nf2*$^{-/-}$ SCs expanded to form solid spheres in which pS6+ cells were distributed throughout (Fig. 6C,D, Supplementary Fig. 7). In contrast, when deprived of Nrg1, pS6+ cells became restricted to the outer perimeter of the spheres in a striking example of spatially patterned heterogeneity (Fig. 6C,D). Consistent with the idea that it is triggered by auto/paracrine Nrg1, pS6 levels in these spheres were blocked by the pan-ErbBi afatinib but not the EGFR-specific inhibitor erlotinib, which actually interfered with the spatial patterning of pS6 itself (Fig. 6E,F). Moreover, this peripherally restricted distribution of pS6+ cells was eliminated by exogenous TGFα or an external polarizing cue provided by functionalizing the PEG hydrogels with integrin-binding RGD peptides (Fig. 6G). In fact, the combination of exogenous TGFα and RGD peptides suppressed pS6 activity altogether and instead strongly induced pNDRG, an effector of basal integrin signaling in normal SCs (Fig. 6G-I)[14]. Thus *Nf2*$^{-/-}$ SCs can self-generate heterogeneous cellular

patterns according to biomarkers of the phenotypic states that we identified in standard cell culture and those patterns are influenced by both auto/paracrine ligands and polarizing external cues.

Quantitative analysis of self-generated heterogeneity in schwannoma

Next, we looked for evidence of self-generated heterogeneity in schwannoma tissue. We developed a quantitative pipeline to study schwannoma heterogeneity by immunofluorescence (IF)-based antibody staining of formalin-fixed paraffin-embedded (FFPE) sections, whole slide scanning of the entire tumor section, and digital image analysis using HALO™ software. Quantitative analysis of the distribution of NRG1, pS6 and pNDRG in tissue sections from four different human vestibular schwannomas (VS) revealed that each exhibited striking intra- and inter-tumoral heterogeneity (Fig. 7A,B, Supplementary Fig. 8A). Visual examination of the scanned tumor tissue revealed that the tumors exhibited large regions that were positive and negative for each biomarker (Fig. 7A, Supplementary Fig. 8A,B). Spatial analysis confirmed that, as predicted by our *in vitro* studies, there was strong regional concordance between Nrg1 and pS6, and discordance between NRG1/pS6 and the basal biomarker pNDRG (Fig. 7C-E, Supplementary Fig. 8B,C). Interestingly there was often a striking demarcation between NRG1+/pS6+ and pNDRG+ regions within a given tumor (Fig. 7E).

To understand how regional patterns of heterogeneity develop in schwannoma, we analyzed *Postn-Cre;Nf2*$^{flox/flox}$ mice[55]. We found that in these mice schwannomas develop synchronously in each of 15 pairs of dorsal root ganglia (DRG) between 3 and 6 months of age (Fig. 8A), providing a unique opportunity to study the evolution of both intra- and inter-tumoral heterogeneity. We first examined Nrg1 and TGFα in DRG lesions in a 6 month-old *Postn-Cre;Nf2*$^{flox/flox}$ mouse at single-cell resolution, applying a Random Forest machine learning algorithm to exclude large DRG soma, which nevertheless served as important geographical landmarks (Fig. 8B). This analysis revealed *intra*-lesion heterogeneity for both Nrg1 and TGFα at this early timepoint (Fig. 8B,C). Importantly, simultaneous analysis of the distribution of Nrg1

and TGFα protein and mRNA by fluorescent *in situ* hybridization-immunofluorescence (FISH-IF) revealed excellent concordance, suggesting that the patterns of ligand distribution are mostly due to autocrine expression and that diffusion of the secreted ligands in the tumor tissue has minimal impact on these patterns (Supplementary Fig. 9A,B). Co-staining of mRNA-identified cell subpopulations revealed broad anti-correlation between *Nrg1*- and *Tgfa*-expressing cells and inter-lesional heterogeneity for these populations across DRG, while also confirming the existence and heterogeneous distribution of cells expressing neither or both *Nrg1* and *Tgfa* (Fig. 8D, E, Supplementary Fig. 9C,D). Notably, analysis by both IF and FISH-IF revealed a spatial bias of Nrg1+ cells in proximity to neuronal soma; pS6 also exhibited a soma-proximal bias, while pNDRG1 localized farther away from soma (Fig. 8F,G; Supplementary Fig. 9E). Finally, zooming in revealed striking spatial patterns of both protein and mRNA within tumor substructures. Cellular 'whorls', which are prominent features of early schwannoma lesions in this model and in human NF2 patients, exhibited concentric patterns of biomarker distribution, with Nrg1/*Nrg1*+ and pS6+ cells often concentrated in the central portion and even 'bullseye', and *Tgfa*+ and pNDRG+ cells at the whorl periphery (Fig. 8H, Supplementary Fig. 9B,F). Altogether these observations highlight the concept of self-generated heterogeneity as an early step in tumorigenesis and the value of this model and approach to understanding it.

Discussion

Heterogeneity has emerged as a central challenge to the successful treatment of many human tumor types and until recently was thought to be driven entirely by underlying genetic variation and consequent tumor:microenvironment interactions[67,68]. Recent studies, particularly of diffuse gliomas of the central nervous system, have uncovered important epigenetic contributions to tumor heterogeneity but how they arise are poorly understood[69-71]. Heterogeneity is also a major issue in schwannoma despite the benign nature and unique genetic homogeneity of these common tumors; it is currently not possible to predict schwannoma growth rate, impact on nerve function, or therapeutic response, rendering clinical

management difficult. While understanding the underpinnings of schwannoma heterogeneity is essential for improving therapeutic options for these patients, the genetic simplicity of schwannomas also provides a unique window into the broadly important contribution of intrinsic mechanisms to tumor heterogeneity.

Our studies suggest that the ability of *Nf2*$^{-/-}$ SCs to variably enact distinct programs of ErbB ligand production and cytoskeletal polarity upon loss of axonally-provided nutrients is a key intrinsic driver of schwannoma heterogeneity. This would be consistent with the variable activation of multiple signaling pathways in *Nf2*$^{-/-}$ SCs, including mTORC1, mTORC2 and YAP/TAZ[22,30,36]. Indeed, while the mTORC1 effector pS6 is induced only when auto/paracrine Nrg1 is available, known SC YAP/TAZ targets *Itga6* and *Dag1* are elevated only upon Nrg1-deprivation, which hyperactivates the basal polarity program, consistent with the well-known activation of YAP/TAZ in response to cell-ECM attachment (Fig. 3F)[72,73]. Variability in the contribution of these 'states' and their distinct auto/paracrine signaling and metabolic programs to each tumor could underlie the heterogeneous clinical behavior and therapeutic response of schwannomas. For example, metabolic dysfunction in glial cells is known to cause neurodegeneration and our studies suggest that heterogeneous metabolic programming is a feature of schwannoma that could differentially impact adjacent nerves[15,21]. Differential signaling triggered by the two polarity 'states' could also explain the heterogeneous therapeutic responsiveness seen for mTORC1- and EGFR-inhibiting drugs in schwannoma patients[6,8]. Our discovery that pS6 is a biomarker of Nrg1 expression but *not* of mTORi sensitivity in cultured *Nf2*$^{-/-}$ SCs, together with the observation that mTORi does not block Nrg1 expression itself while ErbBi does, speaks to the complex clinically relevant circuitry that drives the development of these genetically simple tumors. It will be important to determine whether this complexity is exacerbated by the ability of schwannoma cells to adapt to signaling blockades. It is interesting to note that auto/paracrine Nrg1 expression has been recently reported in *NF2*-mutant meningioma, but in this case is blocked by mTORi, revealing cell-type specific signaling circuitry[74].

A deeper mechanistic understanding of how unstable polarity triggers differential auto/paracrine ligand expression as schwannomas initiate and evolve requires a way to monitor it spatially in 3D and in association with nerves. *In vivo,* intrinsic SC polarity is spatially informed by contact between the apicojunctional surface and the axon, and the two polarized SC surfaces are balanced by unknown mechanisms of feedback[14]. Unstable polarity may disable this feedback mechanism, yielding progressive loss of axonal contact and the acquisition of cell-cell or basal lamina contact and associated auto/paracrine ligand production in an essentially stochastic manner. On the other hand, schwannomas predominantly form on sensory nerves, of which there are many subtypes; the striking sensitivity of *Nf2*$^{-/-}$ SCs to glutamine-glutamate availability suggests that schwannoma initiation and evolution may be biased by the nerves that they are in contact with. Overall, the self-generating design principle we propose here likely also applies to genetically complex tumors, including epithelial cancers that exhibit variable polarized cell architecture, and gliomas, in which unbiased single cell approaches have uncovered tumor cell subpopulations of distinct epigenetic states that may be related to those we identified through hypothesis-driven investigation[70,71].

The unique availability of a mouse model in which multiple *Nf2*-mutant schwannomas develop synchronously in anatomically defined locations provides an opportunity to quantitatively and deeply study schwannoma heterogeneity. By imaging and analyzing multiple lesions in a single mouse, we captured the power of this model to both confirm and extend aspects of our *in vitro* studies. In addition to validating *Nrg1*/Nrg1 and *Tgfa*/Tgfα mRNA and protein as anticorrelated biomarkers of schwannoma heterogeneity, we found a spatial bias of Nrg1-expressing cells within lesions in proximity to DRG soma, a source of Nrg1 that could drive the feedforward Nrg1 expression that we see *in vitro*. Notably, it has been reported that neuronal Nrg1 levels are reduced by *NF2* haploinsufficiency in some nerves, and that Nrg1 can trigger phosphorylation of the Nf2 protein merlin in Nf2-expressing SCs, both of which could further contribute to schwannoma complexity in NF2 patients[45,47]. Our studies set the stage for a comprehensive analysis of how intrinsic tumor heterogeneity evolves over time, and how

stromal, endothelial and immune cell types are spatially recruited to expanding schwannomas. Additional biomarkers can be multiplexed to create multivariate 'heterogeneity indices' for schwannoma that could be mapped to both tumor behavior (ie growth rate or nerve dysfunction) and therapeutic response, with the ultimate goals of predicting tumor behavior, guiding treatment strategy and improving therapeutic options for sporadic schwannoma and particularly NF2 patients, for whom few options exist.

Materials and Methods

Mice

The mouse schwannoma cell line was derived from a tumor dissected from a *P0-CreB;Nf2*$^{flox/flox}$ mouse[75,76]. The genetically engineered mouse model *Postn-Cre;Nf2*$^{flox/flox}$ of NF2 schwannomas was generated by breeding *Postn-Cre* and *Nf2*^{flox} mice[75,77]. All mouse strains were maintained on FVB/N genetic background. Mice were monitored twice a week until dissection at 6 or 12 months of age. All animal care and experimentation were performed with the approval of the UCLA Institutional Animal Care and Use Committees under protocol number 2019-042.

Cell culture and reagents

Primary murine SCs were isolated from sciatic nerves of *Nf2*$^{flox/flox}$ adult mice and purified by magnetic sorting as previously described[48,75]. SCs were routinely cultured in N2 medium (DMEM/F12-HAM, 1x N2 supplement (Thermo Fisher), 50 µg/ml gentamicin (Thermo Fisher), 2 µM forskolin (Calbiochem) and 10 ng/ml Nrg1 (HRG-beta-1 EGF domain) (R&D Systems) on poly-L-lysine (50 µg/ml, Millipore Sigma) and mouse laminin (10 µg/ml, Thermo Fisher) coated plates and incubated at 37° C and 7.5% CO_2. *Nf2* was deleted from *Nf2*$^{flox/flox}$ SCs via adenovirus infection with Cre-recombinase (Ad5-CMV-Cre). Tumoral SCs from mouse schwannomas were isolated by dispase/collagenase dissociation as described[48] and cultured in DMEM supplemented with 10% fetal bovine serum (FBS), 1x N2 supplement, 50 µg/ml gentamicin, 2 µM forskolin, and 10 ng/ml Nrg1 on poly-L-lysine and laminin coated plates at 37°

C and 7.5% CO_2. Adenovirus infection was used for *Nf2* re-expression (Ad5-CMV-Nf2^{WT}). 293A cells for adenovirus production (Agilent), and 293T cells for lentivirus production (ATCC) were cultured in 10% FBS-DMEM with 1% penicillin/streptomycin (Thermo Fisher) and incubated at 37° C and 5% CO_2. For 3D cell culture *Nf2*$^{-/-}$ SCs were trypsinized, centrifuged at 200*g* for 5 minutes (min) and resuspended in complete N2 medium. Cells were then added at a concentration of 5.0 x 10^5 cells/ml to a mixture containing 2mM SLO-dextran polymer and 2mM PEG non-cell degradable cross linker in TrueGel 3D buffer, pH 7.2 (TrueGel3D Hydrogel Kit, Millipore Sigma) and plated in an 8 well chamber slide. Where indicated an RGD peptide (sequence - Acetyl-Cys-Doa-Doa-Gly-Arg- Gly-Asp-Ser-Pro-NH_2; Doa = 8-amino-3,6-dioxaoctanoic acid, Millipore Sigma) was added to the cell suspension at a concentration of 0.5 mM. Hydrogels were allowed to gel for 50 min at room temperature before overlaying with N2 medium. Following incubation at 37° C and 7.5% CO_2 for 48 hours (h), complete N2 medium was either replenished or replaced with Nrg1 free N2 medium or Nrg1 free, TGFα-containing N2 medium and incubated for an additional 72 h.

Growth factors and reagents

Nrg1 was used at 10 ng/ml; All other growth factors were obtained from Peprotech. EGF was used at 10 ng/ml; TGFα was used at 10 ng/ml; HGF was used at 50 ng/ml; PDGF was used at 50 ng/ml. Drug pretreatment was as follows: EIPA (Millipore Sigma), 50 μM, 60 min; afatanib (Selleck), 2 μM, 24 h; erlotinib (Selleck), 2 μM, 24 h; everolimus (Selleck), 100 nM, 24 h. These doses were maintained throughout the experiment.

Plasmids and shRNA constructs

The *Nf2*^{WT} expression construct was generated by PCR amplification of the mouse *Nf2* coding region and cloned into a pAdCMV vector as described[39]. The shRNA constructs targeting mouse ezrin (5'-ATTTCCTTGTTATAATCTCCG-3') in a pLKO-puro.1 vector from GE Healthcare

and described in[27]. The control (shScr; (5'-CAGTCGCGTTTGCGACTGG-3') in a pLKO-puro.1 vector was provided by Marianne James (MGH, Boston)[78].

Virus production and infection

Nf2^{WT}-expressing and Cre-recombinase adenoviruses were generated using the AdEasy system (Agilent) as described in[39]. Cells were infected 24 h before the start of the experiment to induce *Nf2* gene expression. An empty adenoviral vector was used as a control (EV). shRNA-expressing lentiviruses were generated by co-transfecting 293T cells with pLKO-puro.1 vectors and the packaging vectors ΔVPR and VSVG (FuGENE, Promega). Viruses were harvested 24-48 h post transfection. shScr or shEzrin expressing lentiviruses were stably expressed in LDCs and selected in 4 µg/ml puromycin.

Antibodies

The following primary antibodies were used: anti-ezrin mouse monoclonal antibody (mAb) (1:500; MA5-13862, Invitrogen); anti-p75 NTR rabbit mAb (1:1000; D8A8, Cell Signaling Technology); anti-N-cadherin mouse mAb (1:500; clone 32, BD Biosciences); anti-β-catenin mouse mAb (1:500; clone 14, BD Biosciences); anti-pAkt (S473) rabbit mAb (IF: 1:100, WB: 1:1000; D9E, Cell Signaling Technology); anti-Akt rabbit mAb (1:1000; 11E7, Cell Signaling Technology); anti-phospho p44/42 (ERK1/2) rabbit mAb (1:1000; D13.14.4E, Cell Signaling Technology); anti-p44/42 (ERK1/2) rabbit pAb (1:1000; 9102, Cell Signaling Technology); anti-ErbB2 rabbit pAb (IF: 1:100; A0485, Agilent), anti-ErbB3 mouse mAb (IF: 1:100, WB: 1:1000; RTJ2, Invitrogen); anti-E-cadherin mouse mAb (1:1000; clone 36, BD Biosciences); anti-actin mouse mAb (1:1000; clone AC-40, Millipore Sigma); anti-merlin rabbit mAb (1:100; D1D8, Cell Signaling Technology); anti-pS6 (S235/236) rabbit pAb (1:100; 2211, Cell Signaling Technology); anti-Nrg1 rabbit pAb (1:100; ab191139, Abcam); anti-TGFα rabbit pAb (1:100; ab9585, Abcam); anti-pNDRG1 rabbit mAb (1:100; D98G11, Cell Signaling Technology). Alexa Fluor 647-phalloidin or Rhodamine-phalloidin (1:500; Thermo-Fisher) was used to label F-actin. Species-

specific secondary antibodies conjugated to Alexa Fluor 488, 555, or 647 (Invitrogen) were used for IF. DAPI (Invitrogen) was used to label nuclei.

Time lapse imaging

60,000 cells per condition were plated and allowed to adhere for 15 min before washing away unbound cells. Images of regions of interest were captured at 20x magnification at time intervals of 5 min between cycles for 24 h. Cells were imaged on a fully automated Nikon TiE microscope (Micro Device Instruments) equipped with a biochamber heated at 37° C and 5% CO_2 as described in[79].

Immunofluorescence microscopy

Cells for immunofluorescence were plated on glass coverslips coated with poly-L-lysine and laminin 24-48 h before staining. Early confluent cells were fixed and stained when ~80% of the coverslip was covered with cells. For late confluent cells, cells were incubated for 24-48 h after reaching early confluence prior to fixation. Cells were fixed in 4% paraformaldehyde in PBS for 15 min at room temperature, then permeabilized in 0.2% Triton X-100 for 10 min. Primary and secondary antibodies were diluted in PBS with 1% BSA and incubated for 1 h at room temperature. Alexa Fluor-Phalloidin was added with secondary antibodies. Coverslips were mounted with Prolong Gold antifade mountant (Thermo Fisher). Cells were imaged with an inverted laser scanning confocal microscope (LSM710; Carl Zeiss) equipped with a 63x oil immersion objective (Plan Apochromat NA 1.4; Carl Zeiss). DAPI was excited with a 405-nm laser line of a diode laser. Alexa Fluor 488, Alexa Fluor 555, and Rhodamine probes were excited with the 488-nm or 514-nm laser line of an argon laser. Texas-Red fluorescent probes were excited with the 561-nm laser line of a helium-neon laser. Alexa Fluor 647 probes were excited with the 633-nm laser line of a helium-neo laser. Images were acquired as single images or z-stacks in sequential mode using ZEN Black software (2012; Carl Zeiss).

Western blotting

Cells were lysed in RIPA buffer (50 mM Tris, pH 7.4, 1% Triton X-100, 1% SDS, 0.5% sodium deoxycholate, 150 mM NaCl, 1 mM EDTA, 1 mM EGTA, and protease inhibitors). Cell debris was cleared by centrifugation (18,000*g* for 10 min at 4°C) and equal amounts of protein were separated by SDS-PAGE, transferred to PVDF membranes, and immunoblotted with primary antibody overnight at 4°C in 5% milk or 5% BSA (phospho-specific antibody).

Macropinocytosis Assays

For *in vitro* assay, cells were plated on poly-L-lysine and laminin coated glass coverslips and incubated for 24-48 h until close to confluent. Cells were starved of serum and/or Nrg1 overnight in either complete growth medium or glutamine free medium. Dextran-488, (Oregon Green 488; 70,000 da, anionic, lysine fixable) or was added to cells along with growth factor when appropriate (0.5 mg/ml) and incubated for 30 minutes at 37° C. Cells were rinsed 3 times with cold PBS and fixed with 4% paraformaldehyde. For the *in vivo/ex vivo* assay, *Postn-Cre;Nf2*$^{flox/flox}$ mice were injected with 250mg/kg FITC-Ficoll (70,000 Da, Millipore Sigma 51731-1G) and dorsal root ganglia (DRG) were dissected 24 h later. Dissected tumors were incubated overnight in N2 growth medium without Nrg1 and then with 1 mg/mL dextran-TMR (10,000 Da, Molecular Probes D1817) for 1 h in complete N2 growth medium with Nrg.1 For the EIPA *ex vivo* assay, DRG were dissected from *Postn-Cre;Nf2*$^{flox/flox}$ mice, incubated 24 h in N2 growth medium without Nrg with DMSO or EIPA (500μM) pretreatment. DRG were then incubated for 30 min in N2 growth medium with Nrg1 and 1 mg/mL dextran-TMR. After treatments, DRG were directly frozen in OCT blocks and sectioned at 8 μm.

EV production and uptake

EVs were harvested as previously described[80] from the conditioned medium of ~1.0 x 10^8 EO771-LMB cells expressing tandem dimer Tomato (tdTomato) fused to the NH2-terminus to a palmitoylation signal (Palm-tdTomato)(kindly provided by Drs. Xandra Breakfield and Shannon

Stott). Medium was collected and centrifuged at 300*g* for 10 min and at 2000*g* for 10 min. Supernatants were filtered (0.8 μm; EMD Millipore) and ultracentrifuged at 100,000*g* for 90 min at 4°C (Optima L-90K Ultracentrifuge, Beckman Coulter). Pelleted EVs were resuspended in 200 µl PBS. EVs were added to cells grown on poly-L-lysine and laminin coated glass coverslips at ~10^6 per 0.7 cm^2 and incubated for 4 h at 37° C. Cells were then fixed and stained with DAPI.

Nutrient deprivation and conditioned medium experiments

Cells were plated in complete N2 medium and allowed to grow for 24-48 h until they reached near confluence. Complete N2 medium was replaced with glutamine-free or Nrg1-free medium, as indicated and incubated for 24 h. For experiments in schwannoma cells serum was also removed from the medium. For glutamate rescue experiments, 10 mM L-glutamic acid (Millipore Sigma) was added to glutamine-free medium and incubated with cells for 24 h. For conditioned medium experiments, medium was harvested from *Nf2*$^{-/-}$ SCs grown on 60 mm plates in complete growth medium, glutamine-free medium, or Nrg1-free medium for 72 h. Medium was centrifuged at 400*g* for 5 min and filtered through a 0.45 µm filter. 100 µl of conditioned medium was added to each coverslip containing *Nf2*$^{-/-}$ SCs for the indicated time.

Quantitative RT-PCR

Total cellular RNA was extracted using TRIzol (Thermo Fisher) and reverse transcribed with MMLV-RT (Promega) using oligo-dT primers. Fast Start Universal SYBR Green mix (Millipore Sigma) was used to amplify 0.5 µl of the RT reaction in a 25 µl total reaction volume. Triplicate samples were run on a Light Cycler 480 system (Roche Applied Science) with cycling conditions of denaturation for 15 seconds at 95° C, annealing for 1 minute at 60° C, and extension at 60° C, 45 cycles. Expression of GAPDH was used as an internal reference gene.
Primer sequences are as follows: *Gapdh* forward (5'-AGGTCGGTGTGAACGGATTTG-3'), reverse (5'-TGTAGACCATGTAGTTGAGGTCA-3'); *Nrg1* forward (5'-

TCATCTTCTAGCGAGATGTCTG-3'), reverse (5'-CAGACATCTCGCTAGAAGATGA-3'); *Nrg1, TypeI* forward (5'- GGGAAGGGCAAGAAGAAGG-3'), reverse (5'-TTTCACACCGAAGCACGAGC-3'); *Nrg1, TypeIII* forward (5'-ACTCAGCCACAAACAACAGAAAC 3'), reverse (5'-GAAGCACTCGCCTCCATT-3'); *Tgfa* forward (5'-CACTCTGGGTACGTGGGTG-3'), reverse (5'-CACAGGTGATAATGAGGACAGC-3'); *Egf* forward (5'-AGCATCTCTCGGATTGACCCA-3'), reverse (5'-CCTGTCCCGTTAAGGAAAACTCT-3'); *Lama2* forward (5'-TCCCAAGCGCATCAACAGAG-3'), reverse (5'-CAGTACATCTCGGGTCCTTTTTC-3'); *Itga6* forward (5'-TGCAGAGGGCGAACAGAAC-3'), reverse (5'-CGTGCTGCCGTTTCTCATATC-3'); *Dag1* forward (5-'CAGACGGTACGGCTGTTGTC-3', reverse (5'-AGTGTAGCCAAGACGGTAAGG-3'); and *Egfr* forward (5'-GCCATCTGGGCCAAAGATACC-3'), reverse (5'-GTCTTCGCATGAATAGGCCAAT-3').

Immunohistochemistry and tissue staining

Immunofluorescence staining was performed on frozen sections dissected from *Postn-Cre;Nf2*$^{flox/flox}$ mice using a standard protocol: after air drying the frozen sections, they were fixed in formaldehyde 3.7% for 15 min, washed in PBS 3 times, incubated in a blocking/ permeabilization buffer (PBS+5%NGS+0.3%Triton) for 1 h. Sections were then incubated with primary antibodies overnight at 4ºC, washed with PBS 3 times and incubated with secondary antibodies for 1 h at room temperature. Nuclear staining was performed with Hoechst 33258 (0.2µg/µL) and sections were mounted with Fluorescence Mounting Medium (Dako S3023). For staining of macropinocytosis assays, slides were washed quickly in PBS before fixation to reduce nonspecific background and then incubated with Hoechst before coverslip mounting[81]. Images were acquired as single-plan in sequential mode using a SP8 Light-Sheet confocal microscope and the LAS X software (Leica). The human samples were collected and analyzed under the David Geffen School of Medicine at UCLA IRB protocol 10-000655. Standard protocols were used for immunofluorescent staining of formalin fixed paraffin embedded human

and mouse tissue. Briefly, tissues were dewaxed in xylene and rehydrated, followed by antigen retrieval in citrate buffer by incubation for 20 min at 95°C. Sections were then blocked in 5% goat serum, 1% BSA in TBST for 1 h and then incubated with primary antibodies overnight at 4° C. Sections were then washed, incubated with secondary antibodies for 1 h at room temperature, and incubated with DAPI to label nuclei prior to mounting on glass slides with Prolong Gold mounting media. Slides were scanned on a Vectra 3 whole slide scanning microscope (Akoya Biosciences), viewed using Phenochart software, and spectrally unmixed using InForm software.

Fluorescent in situ hybridization-Immunofluorescence (RNAscope) and image analysis

Dorsal root ganglion were dissected from a 12-month old *Postn-Cre;Nf2*$^{flox/flox}$ mouse. Formalin-fixed paraffin-embedded tissue sections (3.5 µm) were stained following the Integrated Co-Detection Workflow combining in situ hybridization using the RNAscope Multiplex Fluorescent v2 assay (ACD, Advanced Cell Diagnostics) and immunofluorescence. After preparation of tissues according to the manufacturer's recommendations (Protocols 323100-USM and MK 51-150/Rev B), sections were steamed for target retrieval (15 min), and incubated with primary antibodies against NRG1 (ab191139, Abcam), TGFa (ab9585, Abcam) or Neurofilament L (NF-L, #2837, Cell Signaling Technology) overnight at +4ºC. Protease Plus was applied to the slides (30 minutes) and hybridization was performed using mouse Nrg1 (Cat# 418181, ACD) and Tgfa (Cat# 435251-C2, ACD) probes or RNAscope 3-plex Positive and Negative Control Probes. Opal dyes 520, 570 (FP1487001KT and FP1488001KT Akoya Biosciences) were used for signal development of the RNA probes. Then, NRG1 and TGFa primary antibodies were detected with HRP-conjugated antibody (ARR1001KT, Akoya Biosciences) and TSA-based amplification with Opal dye 690 (FP1497001KT, Akoya Biosciences). NF-L primary antibody was detected with a Alexa Fluor Plus 647-conjugated goat anti-rabbit IgG (H+L) secondary antibody (A32733, Invitrogen). Tissues were counterstained with DAPI and whole slide images were obtained using a Vectra Polaris slide scanner with a 40x objective (Akoya Biosciences) and unmixed using

InForm software (Akoya Biosciences). Image analysis was performed using the HALO software v3.4 (Indica Labs) with module FISH-IF V2.1.5. For each staining, a classifier was created to exclude the neurons cell bodies from the analysis of mRNA probes. Nrg1 and Tgfa mRNA expression was measured using the semi-quantitative ACD scoring. Briefly, the number of dots/ cell was assessed using the HALO FISH-IF module and cells categorized following ACD recommendations as Class 0 (0 dots/cell), Class 1 (1-3 dots/cell), Class 2 (4-9 dots/cell), Class 3 (10-15 dots/cell) or Class 4 (>15 dots/cell). Proximity analysis was performed with HALO between specific cell subpopulations and the neuron cell bodies, identified by the NF-L IF staining. Density heatmaps were generated using the same scale for the four cell subpopulations (0 to 10 cells per 25μm radius). Heatmaps combining two subpopulations were generated by exporting single-color tinted density heatmaps and merging them using the "darker color" layer blending mode in Photoshop (Adobe).

Image analysis and statistics

ImageJ software (version 2.0, National Institutes of Health) was used for all image processing and analysis. The displayed images were produced from single confocal slices or maximum intensity projections (MIP) of z-stack images. Background was removed with rolling ball background subtraction. Lookup tables were applied to produce final images. Cortical actin and basal ezrin area were defined using the approach described in[82]. Briefly, in z-stack images stained with phalloidin to label F-actin and DAPI to label nuclei, the nuclear midpoint was determined and the F-actin labeled area above was defined as cortical actin and the ezrin labeled region below was defined as basal ezrin area. For ease of quantitation, a single confocal image from the top (cortical) or bottom (basal) region of the cell was used to measure cortical actin or basal ezrin in each image. Each channel was background subtracted and thresholding was used to generate a binary image. The thresholded mask was then used to generate pixel area measurements of the percentage of cortical actin area/total cell area. Total cell area was calculated by measuring the area of a region of interest (ROI) drawn around the

periphery of each cell using the polygon tool. Fluorescence intensity was measured by applying a threshold mask to a ROI and calculating the area of positive signal to the total surface area of the cell, field of view, or region of interest. For cell polarity measurements, cell poles were either counted by hand in time lapse images or the aspect ratio (defined as the length of the major axis of the cell divided by the length of the minor axis of the cell) was calculated using the shape descriptor plugin in ImageJ. Dextran or EV uptake was measured using the analyze particles function to determine the ratio of total particle area to total cell area in threshold images. For quantification of the ex vivo macropinocytosis inhibition by EIPA, analysis was performed with 5 single-plane confocal images per conditions, processed as described in[81]. To quantify pS6 peripheral distribution in 3D spheres, the polygon tool was used to draw a ROI around only the outer layer of cells in a sphere and pS6 levels were measured in thresholded images of the ROI (peripheral). The same process was used to measure pS6 levels in the interior cells in ROIs containing the interior layers of cells. pS6 levels were graphed as the ratio of peripheral to interior pS6+ area relative to total area of the sphere. Whole slide scans of DRG lesions from *Postn-Cre;Nf2*$^{flox/flox}$ mice were imported into HALO™ digital image analysis software version 3.2 (Indica Labs). We then developed a digital image analysis algorithm using the HALO™ multiplex IHC algorithm to achieve single cell segmentation of nucleus and cytoplasm and detect Nrg1 and TGFα at a single cell resolution in DRG lesions. Cell recognition and nuclear segmentation was trained and optimized in three randomly selected regions from each section. Thresholds for positive staining for Nrg1 and TGFα were set using 3 randomly selected regions close to and far from DRG soma. A supervised machine learning algorithm (Random Forest classifier) was trained on three randomly selected regions to recognize tumor cells and exclude DRG soma. For spatial analysis, the HALO™ proximity analysis module was used to measure the percentage of positive cells within a 25 μM radius of DRG soma identified using the classifier algorithm. Data from all analyses was imported into Prism 8 for plotting graphs and statistical analysis. The unpaired two tailed Student's t test was used to compare groups.

Data Availability. The data that support the findings of this study are available from the corresponding author upon reasonable request. Source data are provided with this paper.

References.

1 Evans, D. G. Neurofibromatosis type 2 (NF2): a clinical and molecular review. *Orphanet J Rare Dis* **4**, 16 (2009). https://doi.org:10.1186/1750-1172-4-16

2 Plotkin, S. R. & Wick, A. Neurofibromatosis and Schwannomatosis. *Semin Neurol* **38**, 73-85 (2018). https://doi.org:10.1055/s-0038-1627471

3 Jordan, J. T. & Plotkin, S. R. Benign Intracranial Tumors. *Neurol Clin* **36**, 501-516 (2018). https://doi.org:10.1016/j.ncl.2018.04.007

4 Ardern-Holmes, S., Fisher, G. & North, K. Neurofibromatosis Type 2. *J Child Neurol* **32**, 9-22 (2017). https://doi.org:10.1177/0883073816666736

5 Agnihotri, S. *et al.* The genomic landscape of schwannoma. *Nat Genet* **48**, 1339-1348 (2016). https://doi.org:10.1038/ng.3688

6 Plotkin, S. R. *et al.* Audiologic and radiographic response of NF2-related vestibular schwannoma to erlotinib therapy. *Nat Clin Pract Oncol* **5**, 487-491 (2008). https://doi.org:10.1038/ncponc1157

7 Karajannis, M. A. *et al.* Phase II trial of lapatinib in adult and pediatric patients with neurofibromatosis type 2 and progressive vestibular schwannomas. *Neuro Oncol* **14**, 1163-1170 (2012). https://doi.org:10.1093/neuonc/nos146

8 Goutagny, S. *et al.* Phase II study of mTORC1 inhibition by everolimus in neurofibromatosis type 2 patients with growing vestibular schwannomas. *J Neurooncol* **122**, 313-320 (2015). https://doi.org:10.1007/s11060-014-1710-0

9 Erlandson, R. A. & Woodruff, J. M. Peripheral nerve sheath tumors: an electron microscopic study of 43 cases. *Cancer* **49**, 273-287 (1982). https://doi.org:10.1002/1097-0142(19820115)49:2<273::aid-cncr2820490213>3.0.co;2-r

10 Waggener, J. D. Ultrastructure of benign peripheral nerve sheath tumors. *Cancer* **19**, 699-709 (1966). https://doi.org:10.1002/1097-0142(196605)19:5<699::aid-cncr2820190516>3.0.co;2-h

11 Wippold, F. J., 2nd, Lubner, M., Perrin, R. J., Lammle, M. & Perry, A. Neuropathology for the neuroradiologist: Antoni A and Antoni B tissue patterns. *AJNR Am J Neuroradiol* **28**, 1633-1638 (2007). https://doi.org:10.3174/ajnr.A0682

12 Lewis, D. *et al.* The microenvironment in sporadic and neurofibromatosis type II-related vestibular schwannoma: the same tumor or different? A comparative imaging and neuropathology study. *J Neurosurg* **134**, 1419-1429 (2020). https://doi.org:10.3171/2020.3.JNS193230

13 Stierli, S., Imperatore, V. & Lloyd, A. C. Schwann cell plasticity-roles in tissue homeostasis, regeneration, and disease. *Glia* **67**, 2203-2215 (2019). https://doi.org:10.1002/glia.23643

14 Heller, B. A. *et al.* Functionally distinct PI 3-kinase pathways regulate myelination in the peripheral nervous system. *J Cell Biol* **204**, 1219-1236 (2014). https://doi.org:10.1083/jcb.201307057

15 Wilson, E. R., Della-Flora Nunes, G., Weaver, M. R., Frick, L. R. & Feltri, M. L. Schwann cell interactions during the development of the peripheral nervous system. *Dev Neurobiol* **81**, 464-489 (2021). https://doi.org:10.1002/dneu.22744

16 Lewallen, K. A. *et al.* Assessing the role of the cadherin/catenin complex at the Schwann cell-axon interface and in the initiation of myelination. *J Neurosci* **31**, 3032-3043 (2011). https://doi.org:10.1523/JNEUROSCI.4345-10.2011

17 Chan, J. R. *et al.* The polarity protein Par-3 directly interacts with p75NTR to regulate myelination. *Science* **314**, 832-836 (2006). https://doi.org:10.1126/science.1134069

18 Ozcelik, M. *et al.* Pals1 is a major regulator of the epithelial-like polarization and the extension of the myelin sheath in peripheral nerves. *J Neurosci* **30**, 4120-4131 (2010). https://doi.org:10.1523/JNEUROSCI.5185-09.2010
19 Poliak, S., Matlis, S., Ullmer, C., Scherer, S. S. & Peles, E. Distinct claudins and associated PDZ proteins form different autotypic tight junctions in myelinating Schwann cells. *J Cell Biol* **159**, 361-372 (2002). https://doi.org:10.1083/jcb.200207050
20 Boucanova, F. & Chrast, R. Metabolic Interaction Between Schwann Cells and Axons Under Physiological and Disease Conditions. *Front Cell Neurosci* **14**, 148 (2020). https://doi.org:10.3389/fncel.2020.00148
21 Salzer, J. L. Schwann cell myelination. *Cold Spring Harb Perspect Biol* **7**, a020529 (2015). https://doi.org:10.1101/cshperspect.a020529
22 James, M. F. *et al.* Regulation of mTOR complex 2 signaling in neurofibromatosis 2-deficient target cell types. *Mol Cancer Res* **10**, 649-659 (2012). https://doi.org:10.1158/1541-7786.MCR-11-0425-T
23 Garcia-Martinez, J. M. & Alessi, D. R. mTOR complex 2 (mTORC2) controls hydrophobic motif phosphorylation and activation of serum- and glucocorticoid-induced protein kinase 1 (SGK1). *Biochem J* **416**, 375-385 (2008). https://doi.org:10.1042/BJ20081668
24 Boggiano, J. C. & Fehon, R. G. Growth control by committee: intercellular junctions, cell polarity, and the cytoskeleton regulate Hippo signaling. *Dev Cell* **22**, 695-702 (2012). https://doi.org:10.1016/j.devcel.2012.03.013
25 Fehon, R. G., McClatchey, A. I. & Bretscher, A. Organizing the cell cortex: the role of ERM proteins. *Nat Rev Mol Cell Biol* **11**, 276-287 (2010). https://doi.org:10.1038/nrm2866
26 McClatchey, A. I. & Fehon, R. G. Merlin and the ERM proteins--regulators of receptor distribution and signaling at the cell cortex. *Trends Cell Biol* **19**, 198-206 (2009). https://doi.org:10.1016/j.tcb.2009.02.006
27 Hebert, A. M., DuBoff, B., Casaletto, J. B., Gladden, A. B. & McClatchey, A. I. Merlin/ERM proteins establish cortical asymmetry and centrosome position. *Genes Dev* **26**, 2709-2723 (2012). https://doi.org:10.1101/gad.194027.112
28 Gladden, A. B., Hebert, A. M., Schneeberger, E. E. & McClatchey, A. I. The NF2 tumor suppressor, Merlin, regulates epidermal development through the establishment of a junctional polarity complex. *Dev Cell* **19**, 727-739 (2010). https://doi.org:10.1016/j.devcel.2010.10.008
29 Das, T. *et al.* A molecular mechanotransduction pathway regulates collective migration of epithelial cells. *Nat Cell Biol* **17**, 276-287 (2015). https://doi.org:10.1038/ncb3115
30 Yi, C. *et al.* A tight junction-associated Merlin-angiomotin complex mediates Merlin's regulation of mitogenic signaling and tumor suppressive functions. *Cancer Cell* **19**, 527-540 (2011). https://doi.org:10.1016/j.ccr.2011.02.017
31 D'Angelo, R. *et al.* Interaction of ezrin with the novel guanine nucleotide exchange factor PLEKHG6 promotes RhoG-dependent apical cytoskeleton rearrangements in epithelial cells. *Mol Biol Cell* **18**, 4780-4793 (2007). https://doi.org:10.1091/mbc.E06-12-1144
32 Bergert, M. *et al.* Cell Surface Mechanics Gate Embryonic Stem Cell Differentiation. *Cell Stem Cell* **28**, 209-216 e204 (2021). https://doi.org:10.1016/j.stem.2020.10.017
33 De Belly, H. *et al.* Membrane Tension Gates ERK-Mediated Regulation of Pluripotent Cell Fate. *Cell Stem Cell* **28**, 273-284 e276 (2021). https://doi.org:10.1016/j.stem.2020.10.018
34 Morrison, H. *et al.* Merlin/neurofibromatosis type 2 suppresses growth by inhibiting the activation of Ras and Rac. *Cancer Res* **67**, 520-527 (2007). https://doi.org:10.1158/0008-5472.CAN-06-1608
35 Wu, N. *et al.* The Hippo signaling functions through the Notch signaling to regulate intrahepatic bile duct development in mammals. *Lab Invest* **97**, 843-853 (2017). https://doi.org:10.1038/labinvest.2017.29

36 James, M. F. *et al.* NF2/merlin is a novel negative regulator of mTOR complex 1, and activation of mTORC1 is associated with meningioma and schwannoma growth. *Mol Cell Biol* **29**, 4250-4261 (2009). https://doi.org:10.1128/MCB.01581-08
37 Lopez-Lago, M. A., Okada, T., Murillo, M. M., Socci, N. & Giancotti, F. G. Loss of the tumor suppressor gene NF2, encoding merlin, constitutively activates integrin-dependent mTORC1 signaling. *Mol Cell Biol* **29**, 4235-4249 (2009). https://doi.org:10.1128/MCB.01578-08
38 Hamaratoglu, F. *et al.* The tumour-suppressor genes NF2/Merlin and Expanded act through Hippo signalling to regulate cell proliferation and apoptosis. *Nat Cell Biol* **8**, 27-36 (2006). https://doi.org:10.1038/ncb1339
39 Chiasson-MacKenzie, C. *et al.* NF2/Merlin mediates contact-dependent inhibition of EGFR mobility and internalization via cortical actomyosin. *J Cell Biol* **211**, 391-405 (2015). https://doi.org:10.1083/jcb.201503081
40 Chiasson-MacKenzie, C. *et al.* Merlin/ERM proteins regulate growth factor-induced macropinocytosis and receptor recycling by organizing the plasma membrane:cytoskeleton interface. *Genes Dev* **32**, 1201-1214 (2018). https://doi.org:10.1101/gad.317354.118
41 Curto, M., Cole, B. K., Lallemand, D., Liu, C. H. & McClatchey, A. I. Contact-dependent inhibition of EGFR signaling by Nf2/Merlin. *J Cell Biol* **177**, 893-903 (2007). https://doi.org:10.1083/jcb.200703010
42 Cole, B. K., Curto, M., Chan, A. W. & McClatchey, A. I. Localization to the cortical cytoskeleton is necessary for Nf2/merlin-dependent epidermal growth factor receptor silencing. *Mol Cell Biol* **28**, 1274-1284 (2008). https://doi.org:10.1128/MCB.01139-07
43 Maitra, S., Kulikauskas, R. M., Gavilan, H. & Fehon, R. G. The tumor suppressors Merlin and Expanded function cooperatively to modulate receptor endocytosis and signaling. *Curr Biol* **16**, 702-709 (2006). https://doi.org:10.1016/j.cub.2006.02.063
44 Lallemand, D. *et al.* Merlin regulates transmembrane receptor accumulation and signaling at the plasma membrane in primary mouse Schwann cells and in human schwannomas. *Oncogene* **28**, 854-865 (2009). https://doi.org:10.1038/onc.2008.427
45 Schulz, A. *et al.* Neuronal merlin influences ERBB2 receptor expression on Schwann cells through neuregulin 1 type III signalling. *Brain* **137**, 420-432 (2014). https://doi.org:10.1093/brain/awt327
46 Bloomfield, G. & Kay, R. R. Uses and abuses of macropinocytosis. *J Cell Sci* **129**, 2697-2705 (2016). https://doi.org:10.1242/jcs.176149
47 Thaxton, C. *et al.* Schwannomin/merlin promotes Schwann cell elongation and influences myelin segment length. *Mol Cell Neurosci* **47**, 1-9 (2011). https://doi.org:10.1016/j.mcn.2010.12.006
48 Manent, J., Oguievetskaia, K., Bayer, J., Ratner, N. & Giovannini, M. Magnetic cell sorting for enriching Schwann cells from adult mouse peripheral nerves. *J Neurosci Methods* **123**, 167-173 (2003).
49 Newbern, J. & Birchmeier, C. Nrg1/ErbB signaling networks in Schwann cell development and myelination. *Semin Cell Dev Biol* **21**, 922-928 (2010). https://doi.org:10.1016/j.semcdb.2010.08.008
50 Melendez-Vasquez, C. V. *et al.* Nodes of Ranvier form in association with ezrin-radixin-moesin (ERM)-positive Schwann cell processes. *Proc Natl Acad Sci U S A* **98**, 1235-1240 (2001). https://doi.org:10.1073/pnas.98.3.1235
51 Wanner, I. B. *et al.* Role of N-cadherin in Schwann cell precursors of growing nerves. *Glia* **54**, 439-459 (2006). https://doi.org:10.1002/glia.20390
52 Gess, B. *et al.* Inhibition of N-cadherin and beta-catenin function reduces axon-induced Schwann cell proliferation. *J Neurosci Res* **86**, 797-812 (2008). https://doi.org:10.1002/jnr.21528
53 Parrinello, S. *et al.* EphB signaling directs peripheral nerve regeneration through Sox2-dependent Schwann cell sorting. *Cell* **143**, 145-155 (2010). https://doi.org:10.1016/j.cell.2010.08.039

54 Carmona-Fontaine, C. *et al.* Contact inhibition of locomotion in vivo controls neural crest directional migration. *Nature* **456**, 957-961 (2008). https://doi.org:10.1038/nature07441
55 Gehlhausen, J. R. *et al.* A murine model of neurofibromatosis type 2 that accurately phenocopies human schwannoma formation. *Hum Mol Genet* **24**, 1-8 (2015). https://doi.org:10.1093/hmg/ddu414
56 Ha, K. D., Bidlingmaier, S. M. & Liu, B. Macropinocytosis Exploitation by Cancers and Cancer Therapeutics. *Front Physiol* **7**, 381 (2016). https://doi.org:10.3389/fphys.2016.00381
57 Hall, J. *et al.* Delivery of Therapeutic Proteins via Extracellular Vesicles: Review and Potential Treatments for Parkinson's Disease, Glioma, and Schwannoma. *Cell Mol Neurobiol* **36**, 417-427 (2016). https://doi.org:10.1007/s10571-015-0309-0
58 Vader, P., Mol, E. A., Pasterkamp, G. & Schiffelers, R. M. Extracellular vesicles for drug delivery. *Adv Drug Deliv Rev* **106**, 148-156 (2016). https://doi.org:10.1016/j.addr.2016.02.006
59 Armstrong, J. P., Holme, M. N. & Stevens, M. M. Re-Engineering Extracellular Vesicles as Smart Nanoscale Therapeutics. *ACS Nano* **11**, 69-83 (2017). https://doi.org:10.1021/acsnano.6b07607
60 Lee, S. W. *et al.* EGFR-Pak Signaling Selectively Regulates Glutamine Deprivation-Induced Macropinocytosis. *Dev Cell* **50**, 381-392 e385 (2019). https://doi.org:10.1016/j.devcel.2019.05.043
61 Ammoun, S. *et al.* ErbB/HER receptor activation and preclinical efficacy of lapatinib in vestibular schwannoma. *Neuro Oncol* **12**, 834-843 (2010). https://doi.org:10.1093/neuonc/noq012
62 Boucanova, F. *et al.* Disrupted function of lactate transporter MCT1, but not MCT4, in Schwann cells affects the maintenance of motor end-plate innervation. *Glia* **69**, 124-136 (2021). https://doi.org:10.1002/glia.23889
63 Saitoh, F., Wakatsuki, S., Tokunaga, S., Fujieda, H. & Araki, T. Glutamate signals through mGluR2 to control Schwann cell differentiation and proliferation. *Sci Rep* **6**, 29856 (2016). https://doi.org:10.1038/srep29856
64 Giovannini, M. *et al.* mTORC1 inhibition delays growth of neurofibromatosis type 2 schwannoma. *Neuro Oncol* **16**, 493-504 (2014). https://doi.org:10.1093/neuonc/not242
65 Karajannis, M. A. *et al.* Phase II study of everolimus in children and adults with neurofibromatosis type 2 and progressive vestibular schwannomas. *Neuro Oncol* **16**, 292-297 (2014). https://doi.org:10.1093/neuonc/not150
66 Gjorevski, N. & Lutolf, M. P. Synthesis and characterization of well-defined hydrogel matrices and their application to intestinal stem cell and organoid culture. *Nat Protoc* **12**, 2263-2274 (2017). https://doi.org:10.1038/nprot.2017.095
67 Li, Z., Seehawer, M. & Polyak, K. Untangling the web of intratumour heterogeneity. *Nat Cell Biol* **24**, 1192-1201 (2022). https://doi.org:10.1038/s41556-022-00969-x
68 Nicholson, J. G. & Fine, H. A. Diffuse Glioma Heterogeneity and Its Therapeutic Implications. *Cancer Discov* **11**, 575-590 (2021). https://doi.org:10.1158/2159-8290.CD-20-1474
69 Sottoriva, A. *et al.* Intratumor heterogeneity in human glioblastoma reflects cancer evolutionary dynamics. *Proc Natl Acad Sci U S A* **110**, 4009-4014 (2013). https://doi.org:10.1073/pnas.1219747110
70 Neftel, C. *et al.* An Integrative Model of Cellular States, Plasticity, and Genetics for Glioblastoma. *Cell* **178**, 835-849 e821 (2019). https://doi.org:10.1016/j.cell.2019.06.024
71 Patel, A. P. *et al.* Single-cell RNA-seq highlights intratumoral heterogeneity in primary glioblastoma. *Science* **344**, 1396-1401 (2014). https://doi.org:10.1126/science.1254257
72 Poitelon, Y. *et al.* YAP and TAZ control peripheral myelination and the expression of laminin receptors in Schwann cells. *Nat Neurosci* **19**, 879-887 (2016). https://doi.org:10.1038/nn.4316
73 Totaro, A., Panciera, T. & Piccolo, S. YAP/TAZ upstream signals and downstream responses. *Nat Cell Biol* **20**, 888-899 (2018). https://doi.org:10.1038/s41556-018-0142-z

74 Beauchamp, R. L. *et al.* mTOR kinase inhibition disrupts neuregulin 1-ERBB3 autocrine signaling and sensitizes NF2-deficient meningioma cellular models to IGF1R inhibition. *J Biol Chem* **296**, 100157 (2021). https://doi.org:10.1074/jbc.RA120.014960
75 Giovannini, M. *et al.* Conditional biallelic Nf2 mutation in the mouse promotes manifestations of human neurofibromatosis type 2. *Genes Dev* **14**, 1617-1630 (2000).
76 Giovannini, M. *et al.* Schwann cell hyperplasia and tumors in transgenic mice expressing a naturally occurring mutant NF2 protein. *Genes Dev* **13**, 978-986 (1999).
77 Lindsley, A. *et al.* Identification and characterization of a novel Schwann and outflow tract endocardial cushion lineage-restricted periostin enhancer. *Dev Biol* **307**, 340-355 (2007). https://doi.org:10.1016/j.ydbio.2007.04.041
78 James, M. F. *et al.* Modeling NF2 with human arachnoidal and meningioma cell culture systems: NF2 silencing reflects the benign character of tumor growth. *Neurobiol Dis* **29**, 278-292 (2008). https://doi.org:10.1016/j.nbd.2007.09.002
79 Wang, X., Hossain, M., Bogoslowski, A., Kubes, P. & Irimia, D. Chemotaxing neutrophils enter alternate branches at capillary bifurcations. *Nat Commun* **11**, 2385 (2020). https://doi.org:10.1038/s41467-020-15476-6
80 Reategui, E. *et al.* Engineered nanointerfaces for microfluidic isolation and molecular profiling of tumor-specific extracellular vesicles. *Nat Commun* **9**, 175 (2018). https://doi.org:10.1038/s41467-017-02261-1
81 Commisso, C., Flinn, R. J. & Bar-Sagi, D. Determining the macropinocytic index of cells through a quantitative image-based assay. *Nat Protoc* **9**, 182-192 (2014). https://doi.org:10.1038/nprot.2014.004
82 Condon, N. D. *et al.* Macropinosome formation by tent pole ruffling in macrophages. *J Cell Biol* **217**, 3873-3885 (2018). https://doi.org:10.1083/jcb.201804137

Acknowledgments. We thank past and present members of the McClatchey lab for valuable discussions, particularly Christian Davidson for intellectual input in the early stages of this project; Berent Aldikacti for EO771-LMB cells and expertise in EV isolation; João Paulo Oliveira-Costa for advice on HALO-based image analysis; Daniel Irimia and Xiao Wang for assistance with time lapse imaging; MGH Cancer Center/Molecular Pathology Confocal Core for access to confocal microscopy equipment. Confocal laser scanning microscopy was also performed at the Advanced Light Microscopy/Spectroscopy Laboratory and the Leica Microsystems Center of Excellence at the California NanoSystems Institute at UCLA with funding support from NIH Shared Instrumentation Grant S10OD025017 and NSF Major Research Instrumentation grant CHE-0722519. This work was supported by Department of Defense grants W81XWH1910156 and W81XWH210446 (A.I.M, M.G.), a Drug Discovery Initiative Registered Reports Awards from the Children's Tumor Foundation (to A.I.M. 2018-05-005 and J.V. 2020-05-004), and an MGH American Cancer Society Institutional Research Grant (C.C.M.).

Author Contributions. The study was conceived and designed by C.C.M., J.V., M.G., and A.I.M. *In vitro* experiments were carried out by C.C.M., C.H.L., E.F. and E.W. *In vivo* experiments were carried out by J.V. Whole slide scanning and HALO image analysis were carried out by C.C.M, J.V., E.F., and S.L.S. Data were analyzed and interpreted by C.C.M, J.V., C.H.L., M.G., and A.I.M. The project was supervised by A.I.M and M.G. Drafting of the manuscript and preparation of figures was completed by C.C.M, J.V. and A.I.M. All authors read and commented on the manuscript.

Competing interests. The authors declare no competing interests.

Figure Legends

Figure 1. ***Nf2*-deficient Schwann cells exhibit enhanced multipolarity and exaggerated cytoskeletal responses to the presence or absence of Nrg1. A.** Representative phase contrast images of polarity in three independently generated *Nf2*$^{-/-}$ and control parental *Nf2*$^{flox/flox}$ (WT) SC lines. **B.** Quantitation of multipolarity in three *Nf2*$^{-/-}$ and WT SC lines. Data are presented as the fraction of cells containing 2-3 poles or $\geq$ 4 poles. Bars represent SEM for N = 3 independent experiments with n $\geq$ 85 cells per condition. **C.** Quantitation of multipolarity in *Nf2*$^{-/-}$ and WT SC lines as determined by the aspect ratio (length of long axis: length of short axis). Data points represent n = 55 (WT) or n = 50 (*Nf2*$^{-/-}$) cells representative of N = 3 independent experiments. **D**. Confocal images depicting ezrin (magenta) localization in WT and *Nf2*$^{-/-}$ SCs with and without Nrg1 stimulation (10 ng/ml Nrg1, 10 min). Dashed lines outline individual WT or *Nf2*$^{-/-}$ SCs to highlight their aspect ratio. **E**. Violin plot depicting basal ezrin intensity in WT and *Nf2*$^{-/-}$ SCs with and without Nrg1. The area of ezrin-containing microvilli was measured in confocal images of the basal surface of the cell (see methods) by generating

thresholded images of ROIs at the boundary between two cells. Data points represent the ratio of ezrin+ area to total cell area for n = 33 (WT, -Nrg1), n = 30 (WT, +Nrg1), n = 34 (*Nf2*$^{-/-}$, -Nrg1), or n = 31 (*Nf2*$^{-/-}$, +Nrg1) cells and are representative of N = 3 independent experiments. **F.** Confocal images depicting F-actin (green) distribution in WT and *Nf2*$^{-/-}$ SCs with and without Nrg1 stimulation. Dashed lines outline individual WT or *Nf2*$^{-/-}$ SCs to highlight their aspect ratio. **G.** Quantitation of cortical F-actin in WT and *Nf2*$^{-/-}$ SCs with and without Nrg1 stimulation. Cortical actin intensity was determined by measuring the ratio of cortical F-actin area to total cell area in thresholded images of confocal images of the cortical surface of the cell (see methods). Data points depict n = 21 (WT, -Nrg1), n = 27 (WT, +Nrg1), n = 30 (*Nf2*$^{-/-}$, -Nrg1), or n = 30 (*Nf2*$^{-/-}$, +Nrg1) cells and are representative of N = 3 independent experiments. **H.** Quantitation of polarity in *Nf2*$^{-/-}$ SCs infected with shSCR- or shEzrin-expressing lentiviruses as measured by aspect ratio (long to short axis). Data points represent n = 50 cells per condition; N = 2 independent experiments. All data are depicted as mean +/- SEM. All P values were calculated with unpaired two-tailed Student's t-test. ***p<0.001. All scale bars = 10 μm.

Figure 2. **Adhesion and macropinocytosis in *Nf2*$^{-/-}$ SCs in the presence of Nrg1. A.** Confocal images depicting N-cadherin (magenta) and β-catenin (green) localization in Nrg1-stimulated WT and *Nf2*$^{-/-}$ SCs. **B.** Quantitation of polarized N-cadherin intensity in Nrg1 stimulated WT and *Nf2*$^{-/-}$ SCs. Polarized N-cadherin expression was measured by dividing the N-cadherin containing area in a ROI along the longest axis of a cell by the N-cadherin containing area of a ROI of equal size along the shortest axis of the cell. Individual data points representing n = 20 junctions per condition are graphed. N = 3 independent experiments. **C.** *Top,* MIP of z stack of late confluent *Nf2*$^{-/-}$ SCs labelled for F-actin (green). *Bottom,* vertical x-z section of confocal z stack image showing tightly packed cluster of cells that lose contact with the laminin-coated coverslip. **D.** Graph showing duration of sustained contact after WT and *Nf2*$^{-/-}$ SCs collide as calculated from time lapse phase contrast microscopy images. Data points are graphed for n = 22 (WT) or n = 21 (*Nf2*$^{-/-}$) cells**.** N = 3 independent experiments. **E.** Individual

phase contrast images from time lapse microscopy showing the result of collision between WT or *Nf2*$^{-/-}$ SCs. Asterisks mark two individual cells that come into contact. See also Videos S1 and S2. **F.** Uptake of the macropinocytosis cargo dextran-488 with or without Nrg1-stimulation (30 min) in WT and *Nf2*$^{-/-}$ SCs. **G.** Quantitation of dextran-488 uptake in WT and *Nf2*$^{-/-}$ SCs with or without Nrg1-stimulation. n = 37 (WT, -Nrg1), n = 38 (WT, +Nrg1), n = 37 (*Nf2*$^{-/-}$, -Nrg1), or n = 40 (*Nf2*$^{-/-}$, +Nrg1) cells. N = 3 independent experiments. **H.** Graph showing dextran-488 uptake in *Nf2*$^{-/-}$ SCs treated with vehicle (DMSO) or 50 μM EIPA. Data points are shown for n = 24 (WT) or n = 21 (*Nf2*$^{-/-}$) cells**.** N = 3 independent experiments. **I.** Confocal images of macropinocytic uptake of FITC-Ficoll (green; tail vein injected) and dextran-488 (magenta; applied *ex vivo*) in an early DRG lesion in a 12 month-old *Postn-Cre;Nf2*$^{flox/flox}$ mouse. **J.** Confocal images of dextran-TMR uptake with and without EIPA treatment (0.5 mM) *ex vivo* in a DRG lesion from a *Postn-Cre;Nf2*$^{flox/flox}$ mouse. Scale bar = 30μm. **K.** Quantitation of dextran-TMR uptake in a DRG lesion *ex vivo* with and without EIPA treatment. Data points are shown for n = 10 (DMSO) or n = 8 (EIPA) cells, N = 3. **L.** Uptake of Palm-tdTomato-labelled EVs into *Nf2*$^{-/-}$ schwannoma cells after treatment with vehicle (DMSO) or 50 μM EIPA. Data points are shown for n = 40 cells for DMSO, n = 18 cells for EIPA. N = 3 independent experiments. All data are depicted as mean +/- SEM. All P values were calculated with unpaired two-tailed Student's t-test. ***p<0.001. Scale bars = 10 μm unless otherwise indicated.

Figure 3. *Nf2*$^{-/-}$ SCs upregulate basal polarity components upon Nrg1-deprivation. A. Levels of *Nrg1* mRNA in WT and *Nf2*$^{-/-}$ SCs grown in complete medium (control; Con) or deprived of Nrg1 for 24 h. Data is presented as mean +/- SEM relative to WT mRNA levels for 3 replicates, N = 3 independent experiments. B. Levels of *Tgfa* and *Egf* mRNA in WT and *Nf2*$^{-/-}$ SCs grown under complete medium or deprived of Nrg1 for 24 h. Data is presented as mean +/- SEM relative to WT mRNA levels for 3 replicates, N = 3 independent experiments (*Tgfa*); N = 2 independent experiments (*Egf*). **C**. Quantitation of macropinocytic dextran-488 uptake in *Nf2*$^{-/-}$ SCs starved of Nrg1 overnight and stimulated with 10 ng/ml Nrg1, TGFa, or EGF. Data points

are shown for n = 18 (starved), n = 20 (Nrg1), n = 16 (TGFa), or n = 8 (EGF) cells and representative of N = 3 independent experiments. **D.** Confocal images depicting the distribution of F-actin (green) and ezrin (magenta) in *Nf2*$^{-/-}$ SCs starved of Nrg1 overnight and stimulated with 10 ng/ml Nrg1 or TGFa. Scale bar = 10 μm. **E.** Quantitation of cortical actin and basal ezrin in cells in (D). Cortical actin or basal ezrin were measured in single plane threshold images from 3D zstacks as the ratio between actin or ezrin area and total cell area for n = 20 cells per condition. N = 3 independent experiments. **F.** Levels of *Lama2*, *Itga6*, and *Dag1* mRNA in WT and *Nf2*$^{-/-}$ SCs in complete medium or after 24 h Nrg1-deprivation. Data is presented as mean +/- SEM relative to WT mRNA levels for 3 replicates, N = 3 independent experiments. All data are depicted as mean +/- SEM. All P values were calculated with unpaired two-tailed Student's t-test. *p<0.05, ***p<0.001.

Figure 4: *Nf2*$^{-/-}$ SCs enact a distinct feedforward autocrine Nrg1 signaling program upon nutrient deprivation. A. Macropinocytic dextran-488 uptake in WT and *Nf2*$^{-/-}$ SCs in response to 24 h glutamine deprivation with and without treatment with 2 μM ErbBi. Data points are graphed for n = 10 (WT, all conditions), n = 8 (*Nf2*$^{-/-}$, +Q), n = 11 (*Nf2*$^{-/-}$, -Q), or n = 10 (*Nf2*$^{-/-}$, -Q/ ErbBi) cells. N = 3 independent experiments. **B**. Levels of *Nrg1* mRNA in WT and *Nf2*$^{-/-}$ SCs grown for 24 h in complete medium or glutamine-deprived medium (-Q). Data is presented as mean +/- SEM relative to WT mRNA levels for n = 3 replicates. N = 3 independent experiments. **C.** Confocal images of F-actin (green) depicting cortical ruffling in *Nf2*$^{-/-}$ SCs stimulated for 10 min with conditioned medium from glutamine-deprived (-Q) but not glutamine replete (+Q) *Nf2*$^{-/-}$ SCs. Scale bar = 10 μm. **D.** Quantitation of cortical ruffling from cells in (C). Data points are shown for n = 15 (+Q) or n = 18 (-Q) cells. N = 3 independent experiments. **E.** Dextran-488 uptake in *Nf2*$^{-/-}$ SCs stimulated for 30 min with conditioned medium from glutamine replete (+Q) *Nf2*$^{-/-}$ cells or from glutamine-deprived (-Q) *Nf2*$^{-/-}$ cells treated with vehicle (DMSO), 50 μM EIPA, or 2 μM ErbBi. Data points represent n = 15 (+Q), n = 18 (-Q), n =10 (-Q, EIPA), or n = 5 (-Q, ErbBi) cells. N = 3 independent experiments. **F.** Levels of *Nrg1* mRNA in glutamine-deprived (-

Q) *Nf2*$^{-/-}$ SCs with or without the addition of 10 mM L-glutamic acid. Bars represent mean +/- SEM relative to +Q, DMSO mRNA levels for n = 3 replicates. N = 2 independent experiments. All data are depicted as mean +/- SEM. P values were calculated with unpaired two-tailed Student's t-test (D) or one way ANOVA with Tukey's multiple comparisons test (A, B, E, F). ***p<0.001.

Figure 5. Heterogeneous mTOR activation and drug sensitivity A. Confocal images depicting the dramatic induction of pS6 (green) in Nrg1/glutamine-deprived *Nf2*$^{-/-}$ SCs but not WT SCs. Scale bar = 10 μm. **B.** Quantitation of pS6 levels in cells in (A) as measured in thresholded confocal images as the ratio between pS6 area and total cell area. Data points are graphed for n = 12 (WT) or n = 17 (*Nf2*$^{-/-}$) cells per condition. N = 3 independent experiments. **C.** Quantitation of pS6 levels in *Nf2*$^{-/-}$ SCs treated with conditioned medium from glutamine- (-Q) or Nrg1-deprived *Nf2*$^{-/-}$ SCs. Data poinsts are shown for n = 15 (Con.) or n = 12 (-Q, -Nrg1) cells per condition. N = 3 independent experiments. **D.** Quantitation of cell viability of *Nf2*$^{-/-}$ SCs deprived of Nrg1 or glutamine upon treatment with mTORi (100 nM, 72h). Bars represent mean +/- SEM percentage of cells compared to vehicle treatment. n = 3, N = 2 independent experiments. **E. Levels of** *Nrg1* mRNA in glutamine-deprived *Nf2*$^{-/-}$ SCs treated with vehicle (DMSO) or 100 nM mTORi. Data is presented as mean +/- SEM relative to +Q, DMSO mRNA levels for n = 3 replicates. N = 2 independent experiments. **F.** Levels of *Tgfa* mRNA in Nrg-deprived *Nf2*$^{-/-}$ SCs treated with vehicle (DMSO) or 2 μM ErbBi. Data is presented as mean +/- SEM relative to control, DMSO mRNA levels for n = 3 replicates. N = 2 independent experiments. All data are depicted as mean +/- SEM. P values were calculated with unpaired two-tailed Student's t-test (B, D) or one way ANOVA with Tukey's multiple comparisons test (C, E, F). ns = not significant, *p<0.05, **p<0.01, ***p<0.001.

Figure 6. Self-generated heterogeneity. A. Summary graphs depicting levels of *Nrg1* and *Tgfa* mRNA in three independently generated *Nf2*$^{-/-}$ and WT SC lines grown under steady-state conditions (blue) or deprived of Nrg1 (green) or glutamine (magenta) for 24 h. Data is presented as a violin plot where each dot represents fold change of mRNA relative to steady state conditions of the same genotype of an individual replicate and each SC line is represented by a different shade of color (light, medium, or dark). **B.** Summary graphs depicting changes in polarized cytoskeletal organization in *Nf2*$^{-/-}$ and WT SC lines stimulated with either TGFa (green) or Nrg1 (magenta) for 10 min. Data is presented as a violin plot where each dot represents the ratio between actin or ezrin area and total cell area in a single cell in threshold images and each SC line is represented by a different shade of color (light, medium or dark). **C**. Confocal images depicting the differential distribution of pS6 (magenta) in single cell-derived spheres of *Nf2*$^{-/-}$ SCs cultured in polyethylene glycol (PEG) gels in the presence and absence of Nrg1. **D.** Quantitation of the peripheral distribution of pS6 in *Nf2*$^{-/-}$ PEG spheres as measured by the ratio of peripheral (outermost layer of cells) to internal staining (inner layers of cells). Data points represent n = 16 spheres per condition. N = 3 independent experiments. **E.** Confocal images showing pS6 staining of DMSO-, EGFRi- or pan-ErbBi-treated *Nf2*$^{-/-}$ PEG spheres. **F.** Quantitation of total pS6 levels in *Nf2*$^{-/-}$ PEG spheres treated with DMSO, EGFRi or pan-ErbBi. Data is presented as total pS6 per sphere area for n = 13 (DMSO, ErbBi) or n = 12 (EGFRi) spheres. N = 2 independent experiments. **G.** Quantitation of peripheral pS6 distribution (*left*) and total pS6 levels (*right*) in *Nf2*$^{-/-}$ single cell-derived spheres grown in PEG gels formulated with and without RGD peptides (0.5 mM) or treated with TGFα (10 ng/ml). Data points are shown for n = 14 (Con.), n = 15 (RGD), or n = 22 (TGFα) spheres for peripheral distribution and n = 13 (Con.), n = 18 (RGD), n = 24 (TGFα), or n = 15 (RGD, TGFα) spheres for total pS6 levels. N = 2 independent experiments. **H.** Confocal images showing the distribution of pNDRG1 (green) in *Nf2*$^{-/-}$ PEG spheres in the absence (-Nrg1) or presence of both TGFα and RGD peptides. **I.** Quantitation of total pNDRG1 levels in *Nf2*$^{-/-}$ PEG spheres without (-Nrg1) and with TGFα and RGD peptides. Data points are shown for n = 18 (Con.) or n = 19 (RGD, TGFα)

spheres. N = 2 independent experiments. All data are depicted as mean +/- SEM. P values were calculated with unpaired two-tailed Student's t-test (D, I) or one way ANOVA with Tukey's multiple comparisons test (F, G). ns = not significant, ***p<0.001. Scale bars = 20 μm.

Figure 7. Quantitative analysis of self-generated heterogeneity in human schwannoma tissue. A. Segmentation analysis of NRG1, pS6 or pNDRG1 staining across entire serial sections of a representative human vestibular schwannoma (VS1). Scale bar = 1mm. B. HALO-mediated quantitation of percentage of NRG1, pS6 or pNDRG1-positive cells across entire tumor sections of four different human vestibular schwannomas (VS1,2,3,4). **C.** Summary of correlation analysis of NRG1+ and pNDRG1+ cells with pS6 across 3 VS tumor sections (n = 16 ROIs in 5 20x fields of view per tumor) as measured by Pearson correlation coefficient. P value was calculated with unpaired two-tailed Student's t-test *p = 0.0251. **D.** Heatmap showing levels of NRG1 and pNDRG1 relative to pS6 levels as described in **C**. **E.** Confocal images showing the distribution of pS6 and pNDRG1 in VS2. Dotted line depicts the boundary between pS6+ and pNDRG1+ regions of the tumor. Scale bar = 50 μm.

Figure 8. Quantitative analysis of heterogeneity in schwannomas arising in *Postn-Cre;Nf2$^{lox/lox}$* DRG. A. Representative full slide 40x scan of the array of DRG from a 6 month-old *Postn-Cre;Nf2$^{flox/flox}$* mouse stained for TGFα (magenta) and DAPI (cyan). Scale bar = 1 mm. **B.** *Top left*, image of a single DRG lesion from a 6 month-old *Postn-Cre;Nf2$^{flox/flox}$* mouse stained for Nrg1 (magenta) and DAPI (cyan), along with overlay of HALO-mediated segmentation analysis (*right*) depicting Nrg1+ (lime green) and Nrg1- (grey) cells, and neuronal soma (magenta). *Insets*, representative segmentation analyses of Nrg1 expression close to (i) and far away from (ii) DRG soma. *Bottom left,* image of TGFα (green) and DAPI (cyan) staining, along with overlay of HALO-mediated segmentation analysis depicting TGFα+ (lime green) and TGFα- (grey) cells, and neuronal soma (dark green). *Insets* depict segmentation analyses of TGFα expression close to (i) and far away from (ii) DRG soma. Scale bar = 100 μm. **C.** Graph showing

percentage of cells positive for Nrg1 or TGFα in 6 month-old DRG lesions. Each data point represents one DRG (n = 12, Nrg1; n = 15, TGFα). **D.** Quantitation of *Nrg1*+ and *Tgfa*+ mRNA-expressing cells per entire DRG in a 12 month-old *Postn-Cre;Nf2*$^{lox/lox}$ mouse by FISH. Data point represent individual DRG (n = 15). **E.** Pseudocolored representation of the spatial distribution of *Nrg1*+ and *Tgfa*+ mRNA-expressing cells across an individual DRG lesion. Scale bar = 200 µm. **F.** Proximity analysis measuring the percentage of Nrg1+, pS6+, or pNDRG1+ cells located within 25 µm of DRG soma in 6 month old DRG lesions. Each data point represents one DRG (n = 12, Nrg1; n = 14, pS6; n = 17, pNDRG1) G. Proximity analysis measuring the percentage of *Nrg1* mRNA-expressing versus *Nrg1* mRNA non-expressing cells located within 25 µm of DRG soma. Each data point represents one DRG (n = 14). **H.** *Left*, Confocal image of the bulls-eye like distribution of Nrg1+ cells at the center of a whorl in a developing DRG schwannoma lesion. *Right*, counterstaining for β-catenin reveals additional cellular architecture within the whorl. Scale bar = 20 µm. ***$p<0.001$, unpaired two-tailed Student's t-test.

Chiasson-MacKenzie_Figure 1

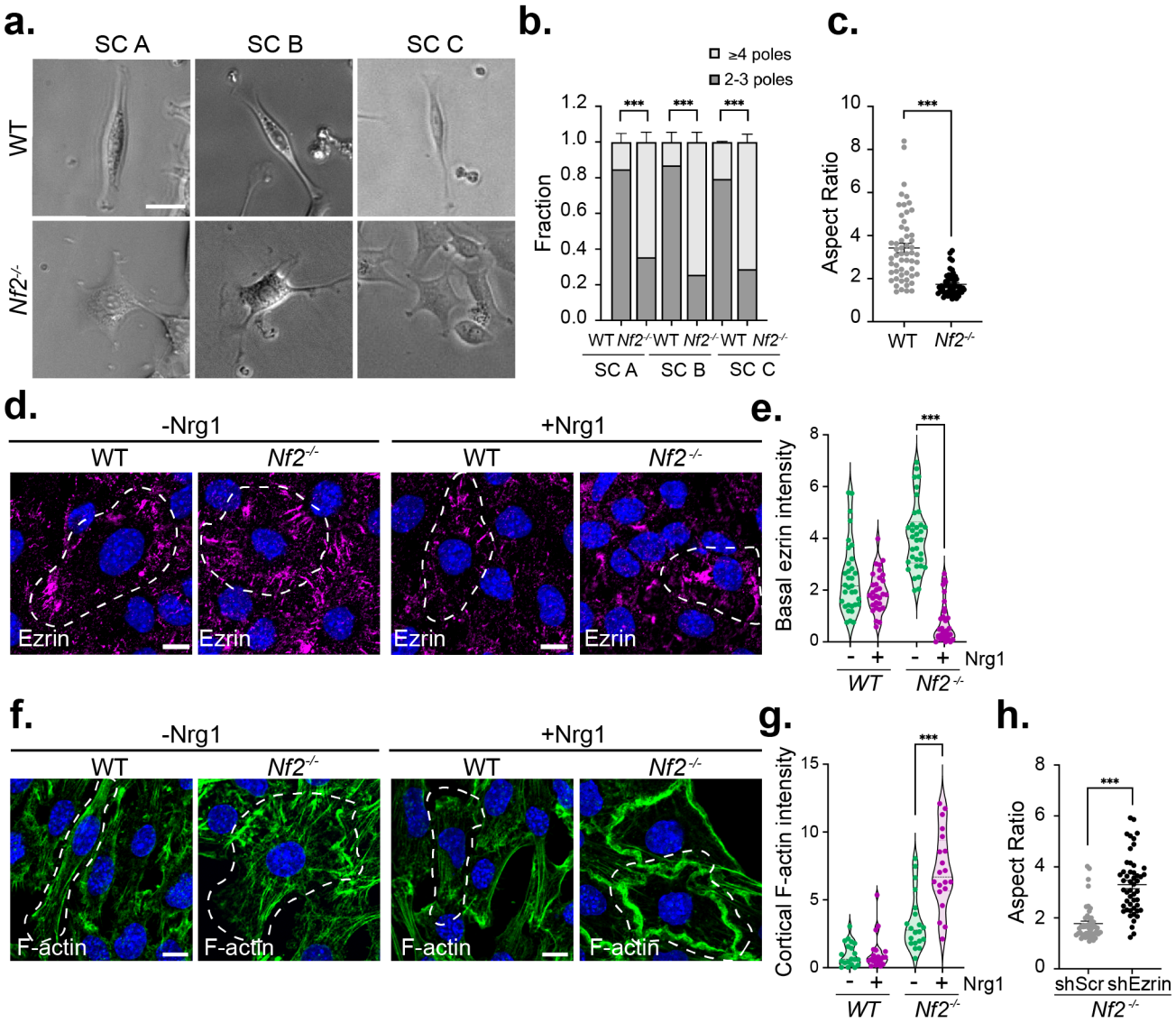

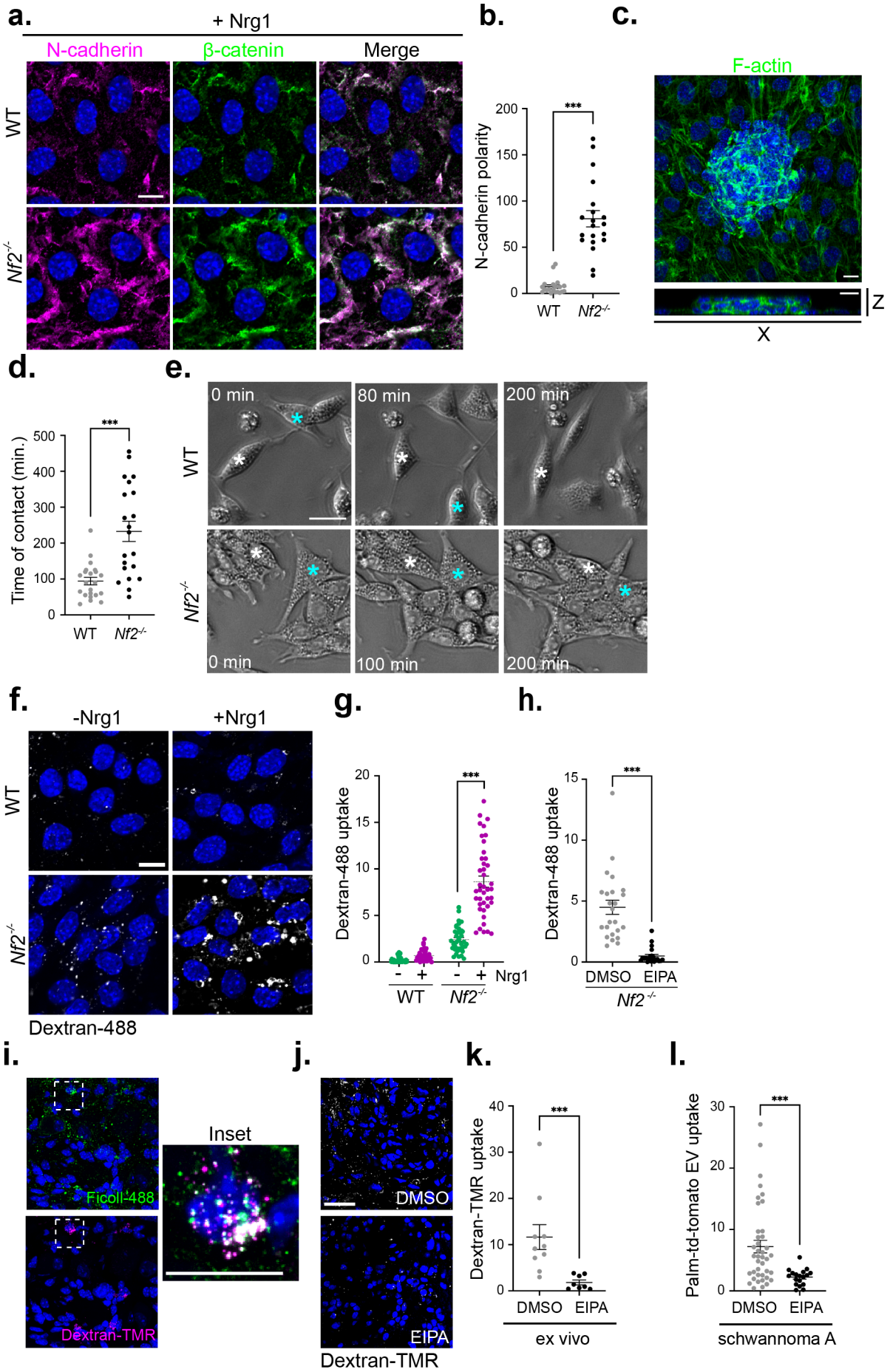
a.
+ Nrg1
N-cadherin
β-catenin
Merge
WT
Nf2-/-
b.
N-cadherin polarity
200
150
100
50
0
***
WT
Nf2-/-
c.
F-actin
Z
X
d.
Time of contact (min.)
500
400
300
200
100
0
***
WT
Nf2-/-
e.
0 min
80 min
200 min
WT
Nf2-/-
0 min
100 min
200 min
f.
-Nrg1
+Nrg1
WT
Nf2-/-
Dextran-488
g.
Dextran-488 uptake
20
15
10
5
0
***
- + - + Nrg1
WT
Nf2-/-
h.
Dextran-488 uptake
15
10
5
0
***
DMSO
EIPA
Nf2-/-
i.
Ficoll-488
Dextran-TMR
Inset
j.
DMSO
EIPA
Dextran-TMR
k.
Dextran-TMR uptake
40
30
20
10
0
***
DMSO
EIPA
ex vivo
l.
Palm-td-tomato EV uptake
30
20
10
0
***
DMSO
EIPA
schwannoma A

Chiasson-MacKenzie_Figure 3

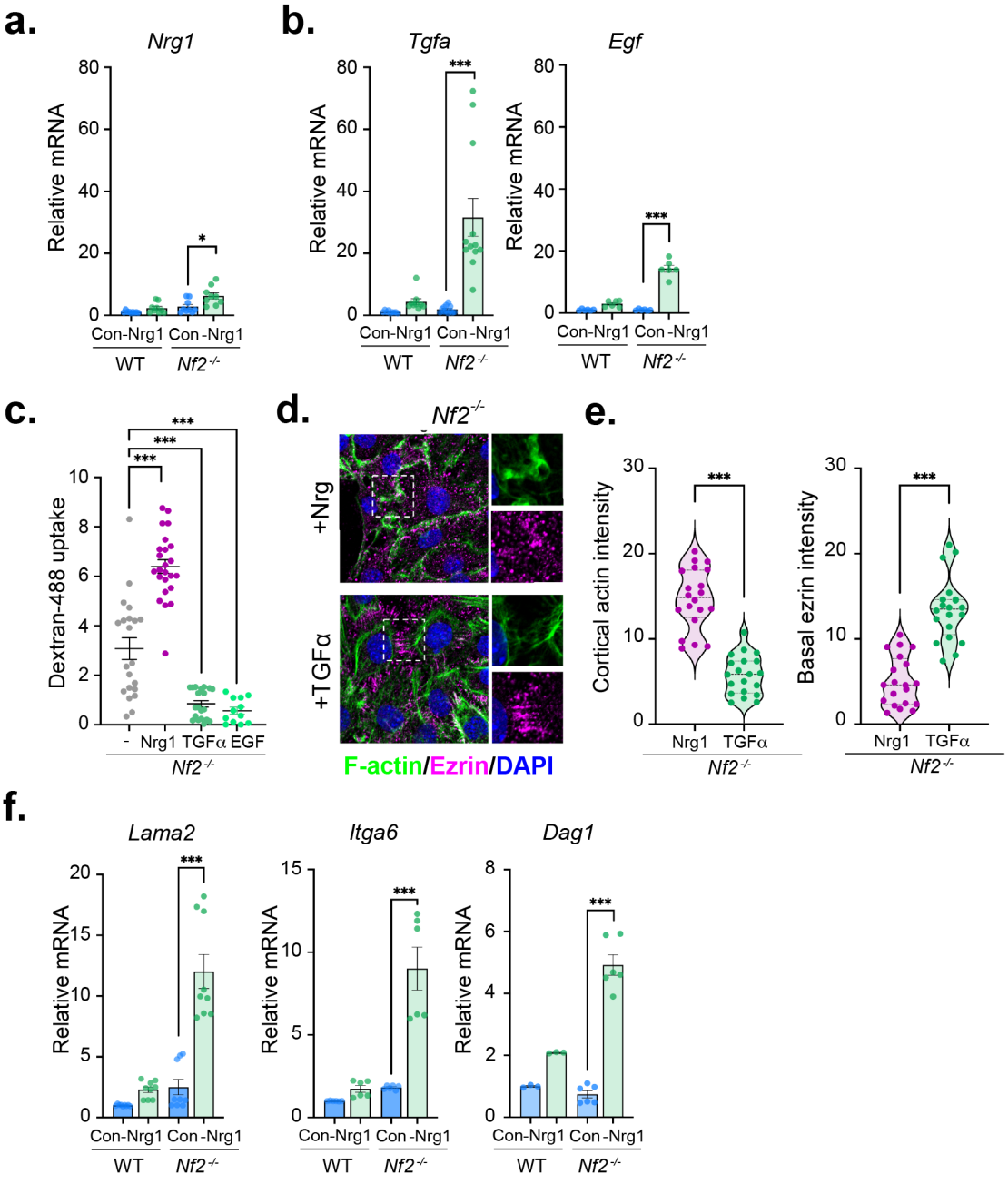

Chiasson-MacKenzie_Figure 4

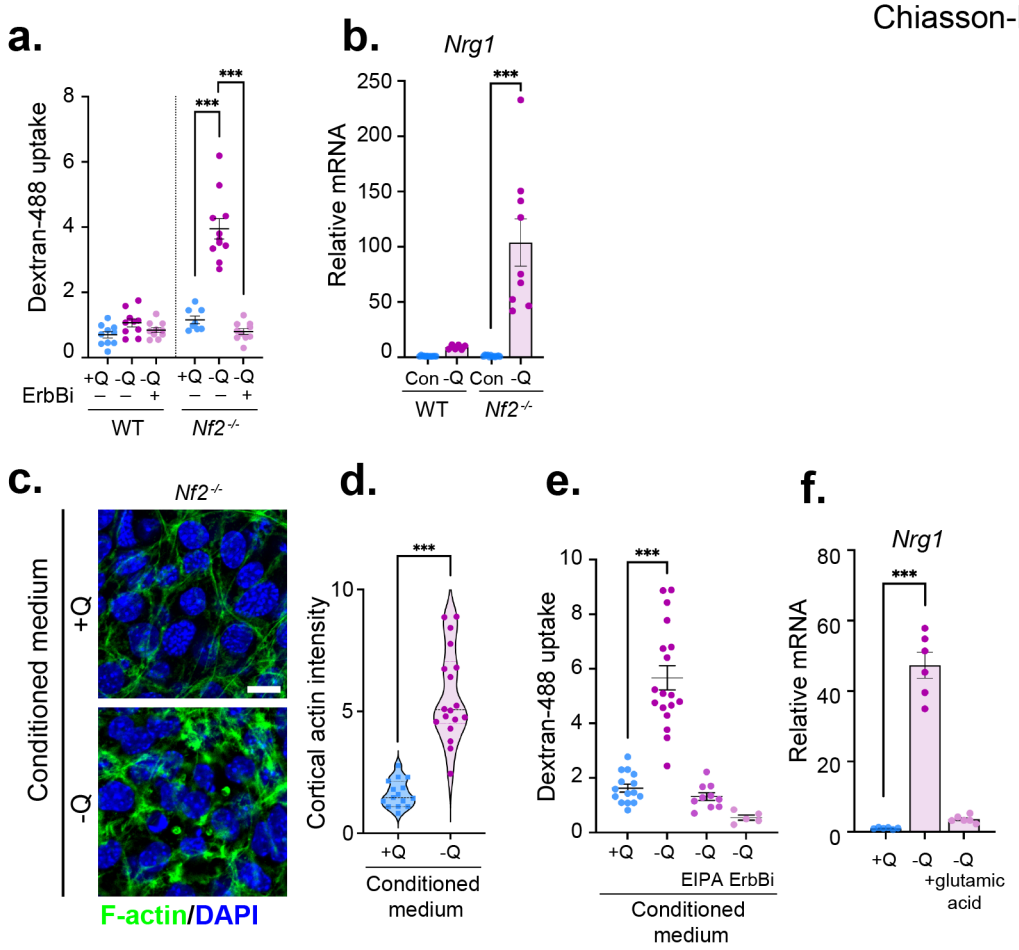

Chiasson-MacKenzie_Figure5

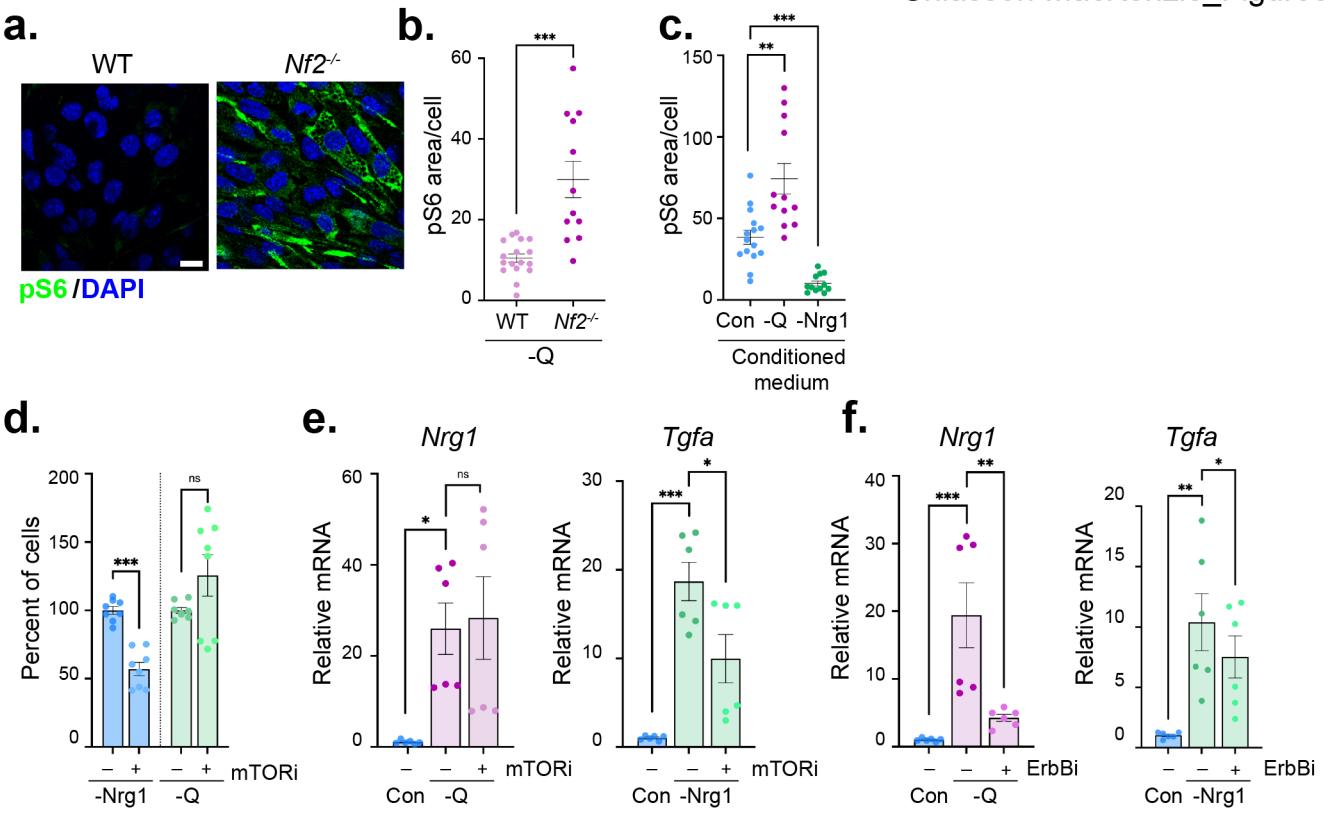

Chiasson-MacKenzie_Figure 6

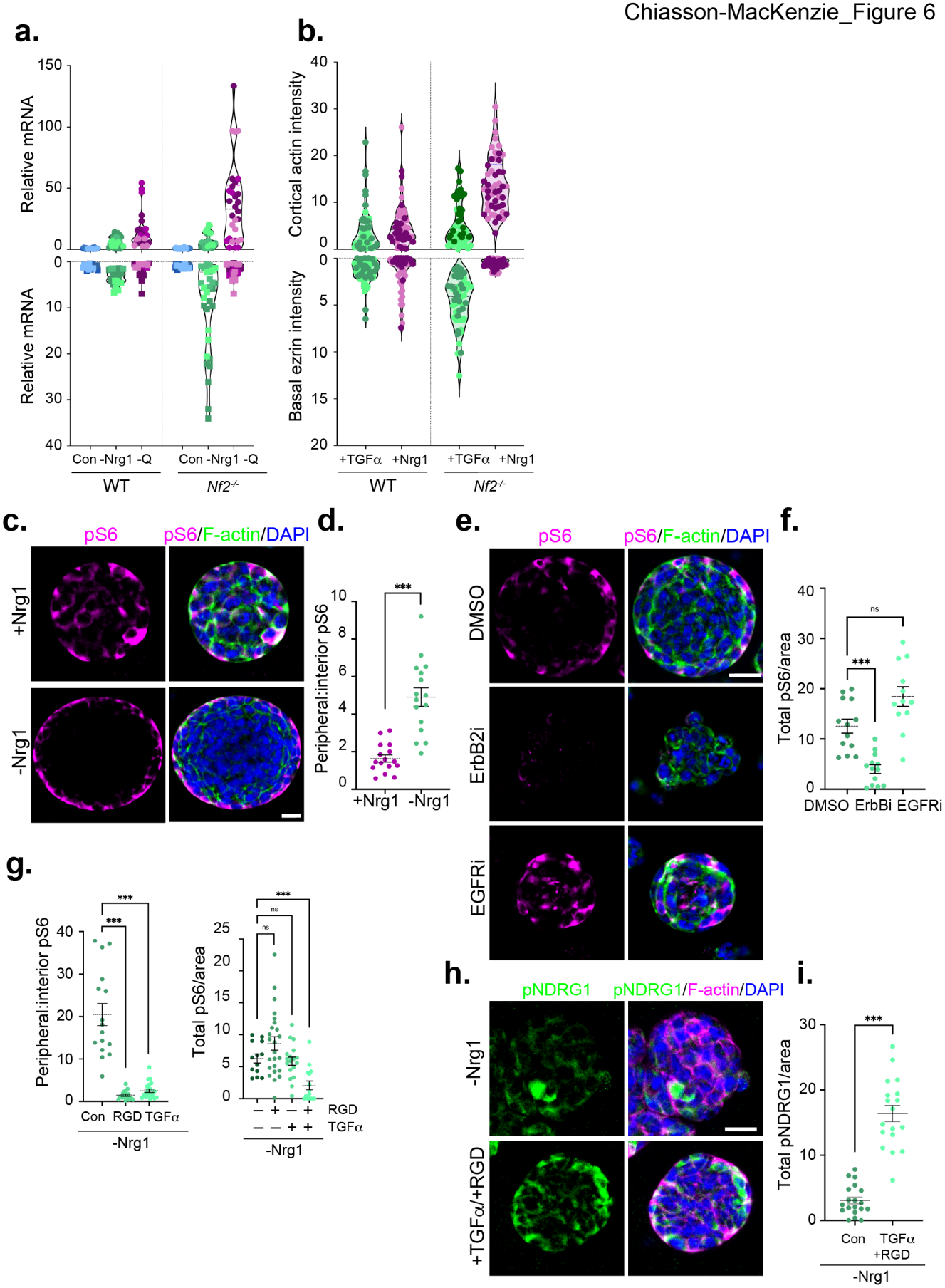

Chiasson-MacKenzie_Figure 7

a.

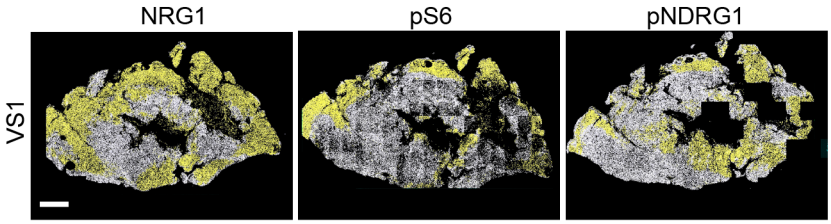

b.

Tumor	Biomarker	% positive cells
VS1	Nrg1	58.4%
VS1	pS6	36.1%
VS1	pNDRG1	34.0%
VS2	Nrg1	12.6%
VS2	pS6	27.6%
VS2	pNDRG1	51.5%
VS3	Nrg1	76.2%
VS3	pS6	27.8%
VS3	pNDRG1	27.5%
VS4	Nrg1	64.7%
VS4	pS6	28.9%
VS4	pNDRG1	43.1%

c.

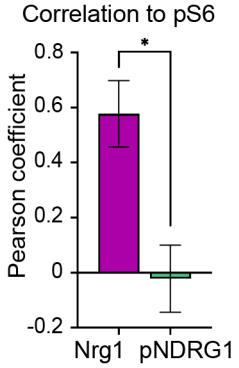

d.

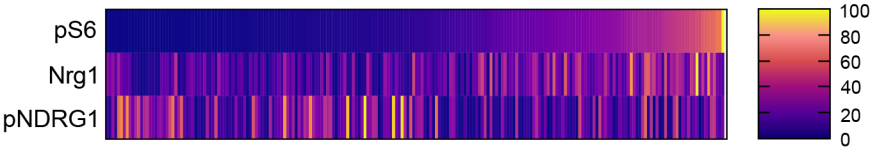

e.

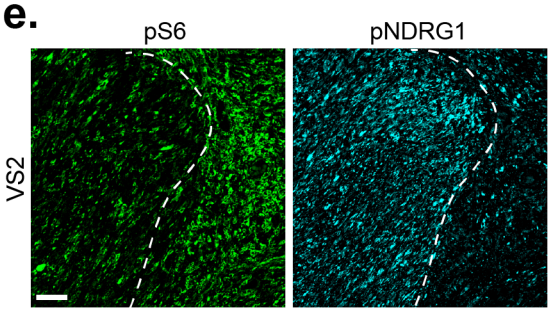
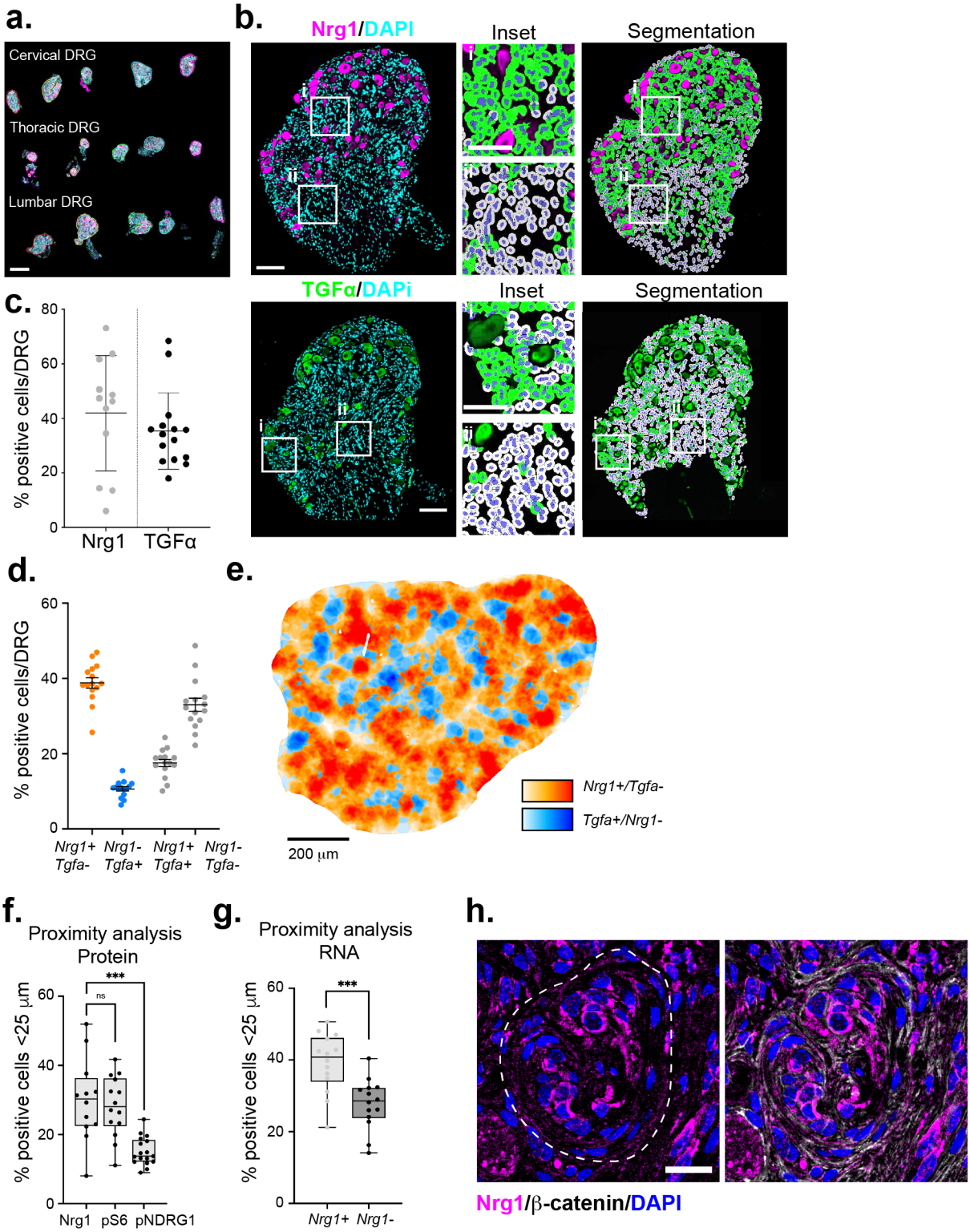
Chiasson-MacKenzie_Figure 8